

# Spatially resolved imaging of the inner Fomalhaut disk using JWST/MIRI

András Gáspár<sup>1\*</sup>, Schuyler Grace Wolff<sup>1</sup>, George H. Rieke<sup>1</sup>, Jarron M. Leisenring<sup>1</sup>, Jane Morrison<sup>1</sup>, Kate Y. L. Su<sup>1</sup>, Kimberly Ward-Duong<sup>2</sup>, Jonathan Aguilar<sup>3</sup>, Marie Ygouf<sup>4</sup>, Charles Beichman<sup>4</sup>, Jorge Llop-Sayson<sup>5</sup> and Geoffrey Bryden<sup>4</sup>

<sup>1</sup>\*Steward Observatory and the Department of Astronomy, The University of Arizona,  
933 N Cherry Ave, Tucson, 85719, AZ, USA.

<sup>2</sup>Department of Astronomy, Smith College, 2 Tyler Ct, Northampton, 01063, MA, USA.

<sup>3</sup>Space Telescope Science Institute, AURA, 3700 San Martin Drive, Baltimore, 21218,  
MD, USA.

<sup>4</sup>Jet Propulsion Laboratory, California Institute of Technology, 4800 Oak Grove Dr,  
Pasadena, 91109, CA, USA.

<sup>5</sup>Department of Astronomy, California Institute of Technology, 1200 E. California Blvd.,  
Pasadena, 91125, CA, USA.

\*Corresponding author(s). E-mail(s): [agasp@arizona.edu](mailto:agasp@arizona.edu);

## Abstract

Planetary debris disks around other stars are analogous to the Asteroid and Kuiper belts in the Solar System. Their structure reveals the configuration of small bodies and provides hints for the presence of planets. The nearby star Fomalhaut hosts one of the most prominent debris disks, resolved by HST, Spitzer, Herschel, and ALMA. Images of this system at mid-infrared wavelengths using JWST/MIRI not only show the narrow Kuiper-Belt-analog outer ring, but also that (1) what was thought from indirect evidence to be an asteroid-analog structure is instead broad, extending outward into the outer system; (2) there is an intermediate belt, probably shepherded by an unseen planet. The newly discovered belt is demarcated by an inner gap, located at  $\sim 78$  au, and it is misaligned relative to the outer belt. The previously known collisionally generated dust cloud, Fomalhaut b, could have originated from this belt, suggesting increased dynamical stirring and collision rates there. We also discovered a large dust cloud within the outer ring, possible evidence of another dust-creating collision. Taken together with previous observations, Fomalhaut appears to be the site of a complex and possibly dynamically active planetary system.

**Keywords:** Debris Disks – Direct Imaging – High Contrast Imaging – Exoplanets – Asteroid belt – Kuiper belt

## 1 Introduction

The Infrared Astronomical Satellite (IRAS) found indications of planetary systems orbiting other stars, in the early 1980s. It was a great surprise that a handful of stars, amongst them Fomalhaut, emitted far infrared radiation well in excess of

their photospheric spectra (Aumann et al, 1984; Gillett, 1986): these infrared signals originated in circumstellar disks of dust and debris. Since then, the detection of thousands of exoplanets and hundreds of debris disks has increased our drive to understand the evolutionary connection

between the planets and debris belts (i.e., asteroidal and Kuiper) of the Solar System with those in extrasolar systems.

Two complementary approaches have advanced our insight to these exoplanetary systems. The first is to study individual assembled and massive planets, either indirectly (e.g. transits and radial velocity oscillations) or by direct imaging. Indirect detections are most efficient close-in, while direct detections are more effective far-out. Transit and radial velocity studies of planet properties are biased against planets even at the Earth-Sun separation, while direct imaging can only reach a bit below the mass of Jupiter at current limits. The second approach, the study of planetary debris disks, focuses on the smallest bodies in a system, the dust and pebbles. Limited by resolving power and/or sensitivity at longer wavelengths and contrast near the central host star at optical/near-IR wavelengths, these studies initially explored the outer zones of the systems. As more powerful instruments have been employed, debris disk studies have increasingly explored inward, and the structures of these disks have the potential to identify moderate-mass planets not identifiable by other means.

Nonetheless, our knowledge of the inner zones of debris disks has been limited: (1) groundbased optical/near-IR telescopes have poor sensitivity to the low surface brightness extended emission of debris disks; while (2) until now, cryogenic space infrared telescopes have had limited spatial resolution and cannot cleanly separate the disk components. JWST overcomes both of these challenges.

In this paper we report deep imaging observations of the debris system around Fomalhaut with JWST/MIRI and the Hubble Space Telescope (HST). A forthcoming paper by Ygouf et al. discusses a deep search for exoplanets in this system using data from NIRCam on JWST. This system brings forth the premier opportunity to resolve many of the questions about debris disks. At  $7.66 \pm 0.04$  pc (van Leeuwen, 2007), it is one of the nearest systems, allowing excellent spatial resolution (e.g., MacGregor et al, 2017). The high stellar luminosity ( $16.63 L_\odot$ ) lights up its debris system ( $L_{\text{IR}}/L_* = 8 \times 10^{-5}$ ; Rhee et al, 2007) and also results in a large physical scale for belts of given temperature. The system was known to host at least two spatially separate components, much

like the Solar System, at similar thermal locations (i.e., at locations where the distance from the star compensates for its luminosity, so there is a similar level of irradiance). The outer Kuiper-belt analog (KBA) component of its disk system (at  $\sim 140$  au, a thermal location of  $\sim 50 - 60$  K) has been imaged in scattered light with HST (Kalas et al, 2005; Galicher et al, 2013; Gáspár and Rieke, 2020), in the thermal infrared with the Spitzer Space Telescope (Stapelfeldt et al, 2004) and the Herschel Space Observatory (Acke et al, 2012), and at radio wavelengths with SCUBA/JCMT and ALMA (e.g., Holland et al, 1998, 2003; Boley et al, 2012; White et al, 2017; MacGregor et al, 2017). These observations have constrained this narrow ring to lie between 136 and 150 au, with a modest eccentricity of  $e = 0.12$ . There is a faint halo of emission outside this belt (Kalas et al, 2005; Espinoza et al, 2011; Acke et al, 2012) due to small grains on highly elliptical orbits or being blown out by photon pressure. An inner warm debris component, an asteroid belt analog (hereafter ABA) at  $\sim 150 - 170$  K (Lebreton et al, 2013; Su et al, 2013; Adams et al, 2018) has also been inferred from the spectral energy distribution (SED), although it has previously not been spatially resolved. The system also exhibits a hot excess originating very close to the star (Absil et al, 2009; Mennesson et al, 2013). Finally, Fomalhaut was identified long ago as a favorable venue for locating exoplanets (Roman, 1959), a suggestion supported by arguments that planets shepherd the debris system (e.g., Quillen, 2006; Chiang et al, 2009; Boley et al, 2012). A planet candidate was identified by Kalas et al (2008), but is more likely to be a dust cloud produced in a massive planetesimal collision (Absil et al, 2009; Lawler et al, 2015; Gáspár and Rieke, 2020).

## 2 Results

We present observations taken with the Mid-Infrared Instrument (MIRI) onboard JWST as well as Cycle 27 (2020-2021) coronagraphic imaging with the Space Telescope Imaging Spectrograph (STIS) onboard HST. Each of these instruments and modes probes different regions and dust sizes, providing a more complete picture of the Fomalhaut planetary system than was previously available. Below, we analyze the features revealed in our JWST observations, as highlighted

## The Architecture of the Fomalhaut Debris Disk System

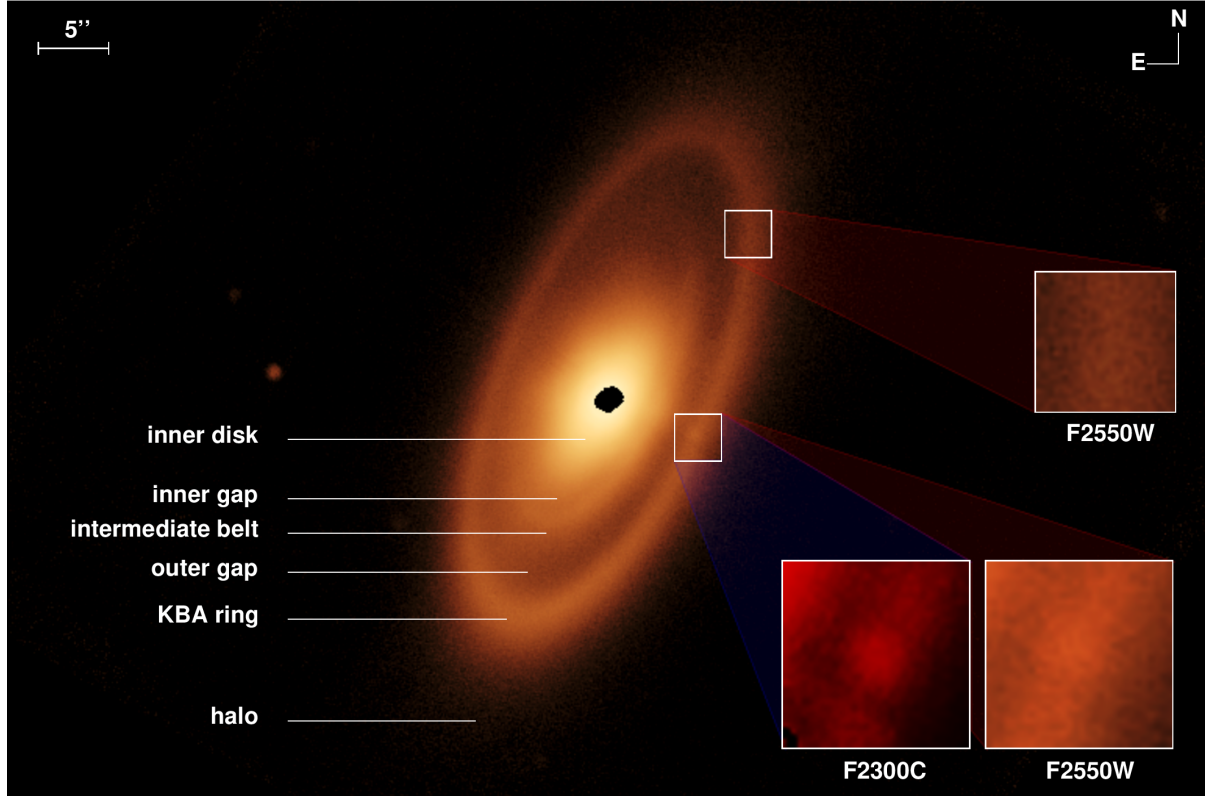


**Fig. 1** We highlight the various features identified in the JWST/MIRI observations of the Fomalhaut system in this  $25.5 \mu\text{m}$  image. The lower two postage stamps enlarge the “Great Dust Cloud” that we identify at  $23.0$  and  $25.5 \mu\text{m}$ , while the upper single postage stamp shows the projected location of Fomalhaut b at the time of the observations (centered on the unbound trajectory solution; see Section “Fomalhaut b”). The  $23.0 \mu\text{m}$  observations did not image this area. Fomalhaut b is not visible in the MIRI imaging.

in Figure 1, showcasing the  $25.5 \mu\text{m}$  JWST image. These include an extended inner disk, an inner gap, an intermediate belt, and a structure within the outer KBA ring we call the “Great Dust Cloud”.

### 2.1 The Asteroid-belt analog

A variety of indirect arguments, based on SEDs and spectra, have identified a relatively warm component to debris disks that appears to be separate from the cold outer KBA rings (e.g., Morales et al., 2011). The Fomalhaut system shares this behavior. Su et al. (2013) found that the SED of the ABA region has a fractional luminosity of  $\sim 2 \times 10^{-5}$  and is well represented by a blackbody of 170 K, suggesting a radial distance of 11 au from the star. This suggests an enticing analogy to the structure of the Solar System, with a cold Kuiper

Belt and a warm Asteroid Belt, with the placement of the belts loosely associated with ice lines in the forming system (Su and Rieke, 2014). Such structures remain by far the most popular explanation for the warmer component of debris disk SEDs in general (Ballering et al., 2014; Kennedy and Wyatt, 2014; Ballering et al., 2017; Geiler and Krivov, 2017). However, inferences about debris disk structure from SEDs can be highly degenerate between the assumed dust grain absorption and emission properties, their distances from the star, scattering phase functions, porosity, sizes, and size-distributions.

The  $15.5$ ,  $23.0$ , and  $25.5 \mu\text{m}$  JWST/MIRI images shown in Figure 2 reveal a disk system that is quite different from previous estimates based on photometry/spectrum fitting alone. The  $25.5 \mu\text{m}$  observations spatially resolve an inner disk structure extending from at least  $\sim 1.^{\prime\prime}2$  ( $\sim 10$  au)

## The JWST Gallery of the Fomalhaut System with Deprojections

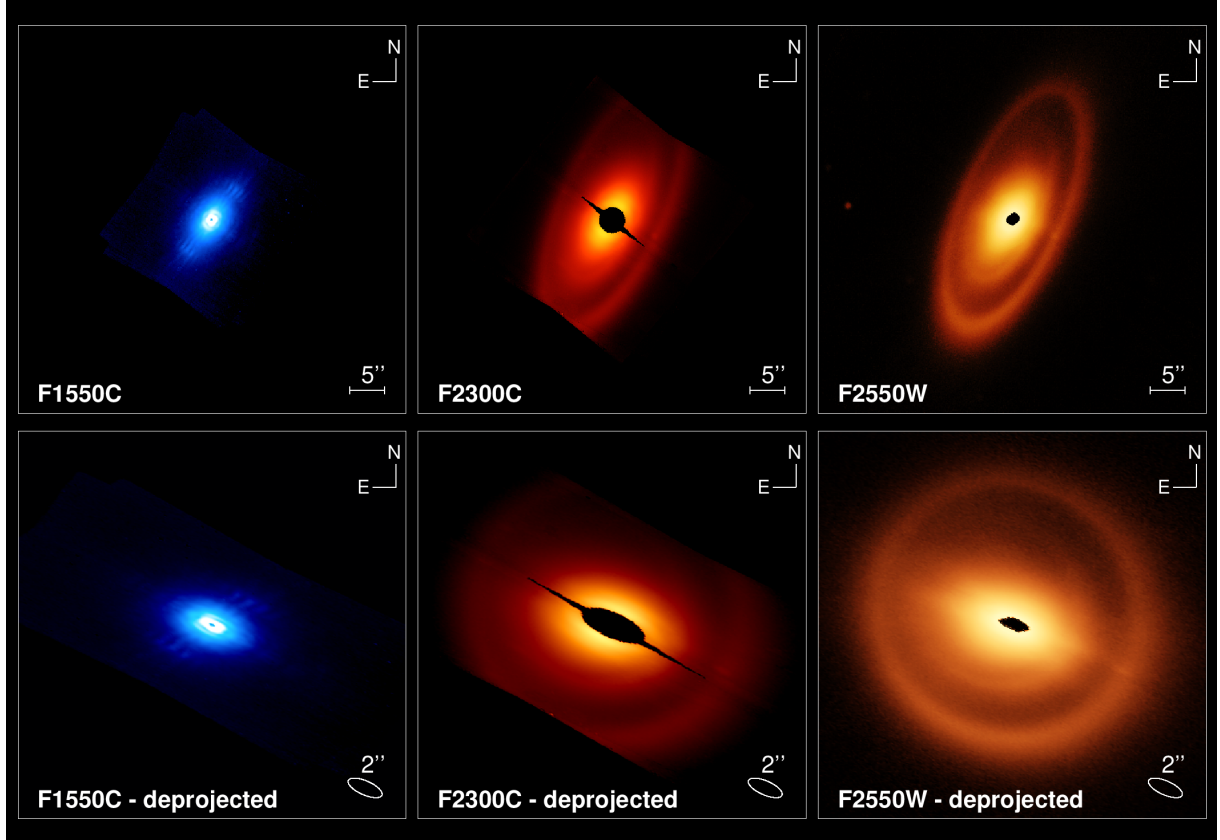


**Fig. 2** JWST observations of the Fomalhaut system at 15.5, 23.0, and 25.5  $\mu\text{m}$ . The top row shows the system at its natural viewing angle, while the bottom row shows the observations deprojected by the best fitting inclination angle. The image scalings, projection fittings, and image reduction steps are discussed in Supplementary Information sections 1 and 2.

outward to  $10''$  -  $12''.5$  (77 au - 96 au; periapsis and apoapsis, respectively), including the intermediate belt. The inner limit ( $\sim 10$  au) is a result of image saturation, but is at the previously estimated location for the ABA component ( $\sim 11$  au; Su et al., 2013). However, the inner disk is significantly more extended radially than was assumed purely from its SED. The extent of this complex inner structure is confirmed at  $23 \mu\text{m}$  as well. The  $15.5 \mu\text{m}$  image is less diagnostic; nevertheless, it shows spatially extended emission tracking well with its longer wavelength counterparts. The “gap” at  $\sim 1''$  in the F1550C data is likely a phase mask PSF subtraction residual, as it is similar to structures seen in commissioning data (Boccaletti et al., 2022). Therefore, the  $15.5 \mu\text{m}$  data is not used to define the boundaries of the inner disk. Both  $23.0$  and  $25.5 \mu\text{m}$  data show a prominent inner gap (see Figure 1 labels) between the inner

disk and the intermediate belt at  $\sim 7''.5$  (periapsis) -  $\sim 14''.2$  (apoapsis), which we discuss in more detail in Section “The intermediate belt”.

In Figure 3, we show the encircled energy at the three observed wavelengths with error bars, in the observed orientation of the system (images in the top row of Figure 2). Due to saturation at the stellar core at  $25.5 \mu\text{m}$  and to the Lyot mask at  $23 \mu\text{m}$ , the flux from the very inner regions is not included in these measurements, although at  $25.5 \mu\text{m}$  we saturate only within  $\sim 1''.2$  ( $\sim 10$  au). We used the position angle (PA) and inclination of the KBA ring, as determined by the MCMC orbit fitting at  $25.5 \mu\text{m}$  (PA =  $336^\circ 28$ ,  $\iota = 67^\circ 52$ ; see Supplementary Information section 2.2), to de-project the images at each observed wavelength (also shown in Figure 2). The de-projection conserved flux; therefore, this view can be used to analyze surface structures as well as

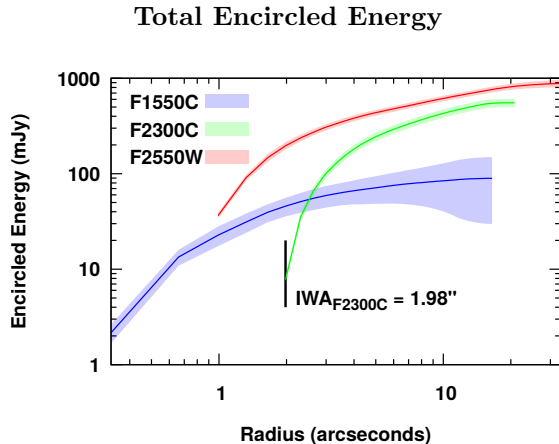


**Fig. 3** The measured total encircled energy at 15.5, 23.0, and 25.5  $\mu\text{m}$  in the observed orientation of the system, as a function of radius. Statistical errors were negligible. The dominant systematic errors are based on PSF subtraction scalings with a conservative 5% and 10% additional error added in quadrature at 25.5 and 23.0  $\mu\text{m}$ , respectively.

to perform photometry on the disk components. In Figure 4, we show the median surface brightness and the encircled energy of the system at the observed wavelengths, as measured on the de-projected images. The calibration of the 23.0  $\mu\text{m}$  data (discussed in the Supplementary Information section 1.2) places it evenly on top of the 25.5  $\mu\text{m}$  data in the outer regions of the system. The total flux of the inner disk – including the intermediate-belt up to 13''.0 – is  $78 \pm 35$  mJy,  $375 \pm 38$  mJy, and  $560 \pm 36$  mJy at 15.5, 23.0, and 25.5  $\mu\text{m}$ , respectively (measured from inner apertures of 0''.5, 2''.3, and 1''.0 in radius, respectively). The spatially extended nature of the inner disk, as resolved at 23.0 and 25.5  $\mu\text{m}$ , explains the low surface brightness and weak detection at 15.5  $\mu\text{m}$  and also contributes to the non-detection of the inner disk with HST/STIS (see Methods and Supplementary Information section 1.3 “Cycle 27 HST Observations”).

The total flux measured at 15.5  $\mu\text{m}$  in the inner region ( $78 \pm 35$  mJy) is less than previously estimated from the Spitzer Infrared Spectrograph (IRS) spectrum (320 mJy with an estimated error per resolution element of 190 mJy, or  $< 60$  mJy smoothed to photometric resolution; Su et al., 2013). We resolve this discrepancy by reviewing the calibration of the IRS data (see details in Supplementary Information section 2.5). The total disk flux, in the recalibrated spectra, is  $102 \pm 60$

mJy at 15.5  $\mu\text{m}$ , and in good agreement with the measurement of  $78 \pm 35$  mJy (Figure 5).

We also can compare the flux from the 25.5  $\mu\text{m}$  image with the recalibrated IRS spectrum. To match the IRS slit dimensions and orientation, we measure the flux in a 12'' wide (and 1' long) box, set at a PA of 64° (Stapelfeldt et al., 2004) in the F2550W image and assign a 10% error. The flux measured within the IRS slit area ( $561 \pm 56$  mJy) lies within the errors, although at a lower flux, than the recalibrated IRS spectrum value at 25.5  $\mu\text{m}$  (Figure 5). The minor discrepancy is likely to indicate a small amount additional flux generated inside a radius of 1''.2 (10 au), which we are missing due to saturation. The small amount of missing flux shows that the disk cannot extend far inside 10 au, nor contain large numbers of small grains ( $\sim 1 \mu\text{m}$ ), or its emission in the  $10 - 17 \mu\text{m}$  range would exceed the limits imposed by the spectrum. In addition, the slope of the surface brightness profile at 25.5  $\mu\text{m}$  in Figure 4 may be decreasing inwards of 2'' compared with further out. These constraints suggest an inner edge in the 7 - 8 au range.

Many debris systems have now been imaged with large ground-based telescopes in scattered light at near-IR wavelengths (e.g., Esposito et al., 2020). At the high resolution of these images, inner dust structures would be readily detected. However, despite the emission from these regions in the 15 - 25  $\mu\text{m}$  range, virtually all of them have inner holes in the near-IR scattered light (to the limits achieved, Esposito et al., 2020). Attempts to image inner structures in optical scattered light with coronagraphs on HST have also been unsuccessful (e.g., Wolff et al., 2023, this paper), nor have they been detected with ALMA (e.g., Su et al., 2016). The low levels of scattered light in the inner Fomalhaut system appear to be a common characteristic. This behavior perhaps arises from minimum grain sizes larger than previously assumed and the resulting low scattering efficiency at near normal incident angles (e.g., Wolff et al., 2023).

Our observations show that the Fomalhaut inner disk system is quite different from that of our own Solar System. While the Asteroid belt is relatively narrow (located between  $\sim 2.1$  and  $3.3$  au), shepherded by a massive planet, the inner region of Fomalhaut hosts an extended disk component. Which architecture is more common? Our

## The Surface Brightness and Encircled Energy in the Deprojected Images.

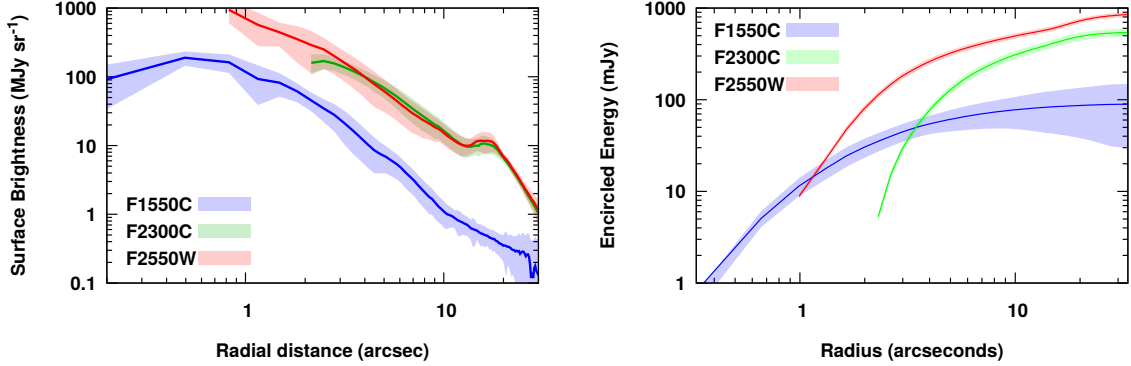


**Fig. 4** *Left panel:* The median surface brightness of the Fomalhaut disk as measured in the de-projected image shown in Figure 2 with pixel standard deviation errors. *Right panel:* The total encircled energy as a function of radial distance as measured in the de-projected images. Measurements inward of  $\sim 1''$  at  $15.5\ \mu\text{m}$  are mostly of PSF subtraction residuals. Statistical errors were negligible. The dominant systematic errors are based on PSF subtraction scalings with a conservative 5% and 10% additional error added in quadrature at  $25.5$  and  $23.0\ \mu\text{m}$ , respectively.

upcoming observations of the Vega and  $\epsilon$  Eridani system and other JWST observations of nearby debris disks should help to steer the discussions on this subject.

## 2.2 The intermediate belt

Perhaps our most intriguing result is the detection of an intermediate belt in the Fomalhaut system. The belt is clearly resolved towards both apices although not nearly as prominently towards the forward direction (N direction as viewed from Earth) of the disk as the back side (S direction as viewed from Earth). This is also true for the outer KBA ring, which is brighter on the southern arc than the northern in thermal imaging. This is opposite to how the system appears in scattered-light HST images, where efficient forward scattering brightens the northern arc.

We fit the inner and outer boundaries of the feature with a Keplerian orbit on the de-projected F2550W image (Figure 2). The outer boundary was the easier one to trace of the two, and has a semi-major axis of  $\approx 104$  au and an eccentricity of  $e=0.265$ . Interestingly, the fitted orbit was inclined by  $i \approx 22.9^\circ$  with respect to the de-projected plane. This agrees with the contour fits (see Supplementary Figure 10), pointing towards an inclination offset between the inner and outer regions. The inner boundary of the feature can be fit with an elliptical path with a semi-major axis of  $\approx 83$  au

## The Recalibrated IRS Spectra and JWST Photometry of the Fomalhaut Debris Disk System.

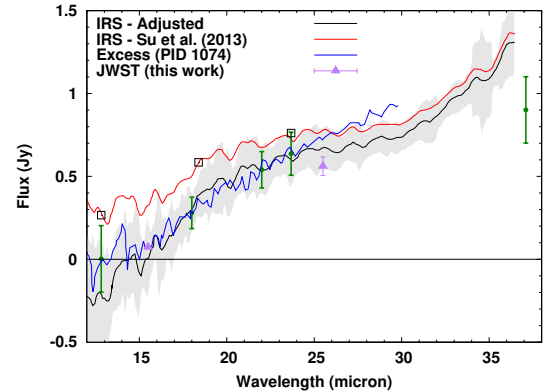


**Fig. 5** The black curve is the spectrum with the calibration adjusted as described in Supplementary Information section 2.5; the green points with  $1\sigma$  error bars show photometry at  $12.8$ ,  $18$ ,  $22$ ,  $24$ , and  $37\ \mu\text{m}$  (see the Supplementary Information for more information). With light gray we plot the  $1\sigma$  errors in the spectrum, including an allowance for uncertainty in the flux of the stellar photosphere (see text). The red curve shows the same data with the previous calibration discussed by [Su et al. \(2013\)](#) and the open boxes are the averages of this spectrum over the photometric bandwidths (1 sigma SD errors in the mean averages are similar to the sizes of the boxes). The blue line is the excess spectrum derived from the data obtained under Spitzer PID 1074. The purple triangles with  $1\sigma$  error bars are from the images at  $15.5$  and  $25.5\ \mu\text{m}$ .

and eccentricity of 0.31. The fitted relative inclination of the inner boundary is much smaller at

$\iota \approx 7.4^\circ$ . The width of the belt varies from ( $\sim 7$  to 20 au). The peak of the belt is at  $\sim 16.8$  MJy sr $^{-1}$  and is  $\sim 1.5$  MJy sr $^{-1}$  above the value of the average background interior and exterior of it.

The feature is demarcated externally by the previously well resolved cleared region, already identified in HST images, and an inner gap in the system, imaged by the JWST/MIRI observations. The inner gap is  $\sim 1.3''$  (10 au) wide at  $\sim 10''$  ( $\sim 78$  au at center) separation from the central star. The gap is clearly present at both 23.0 and 25.5  $\mu\text{m}$  and is therefore a real feature of the system, likely a product of gravitational perturbations from an extrasolar planet. An alternate theory for its presence could be intense dust production at the location of the intermediate belt, resulting for example from the shearing of a recently produced large dust cloud. Detailed numerical modeling of this feature and the characteristics of the shepherding planet will be presented in a follow-up paper; preliminary models using DiskDyn do place upper limits on the mass of the perturbing planet around  $1 M_{\text{Saturn}}$ , which is significantly lower than the detection limits of previous imaging surveys (e.g., [Gauchet et al., 2016](#); [Maire et al., 2014](#); [Kenworthy et al., 2013](#)).

### 2.3 The Great Dust Cloud

An intriguing feature present in both the 23.0 and 25.5  $\mu\text{m}$  observations is a round cloud in the KBA ring, highlighted in Figure 1, which we call the “Great Dust Cloud” (GDC). Since it appears at both wavelengths, it cannot be a reduction artifact. We estimate its brightness to be  $61 \pm 12$   $\mu\text{Jy}$  at 23.0 and  $89 \pm 13$   $\mu\text{Jy}$  at 25.5  $\mu\text{m}$  in excess of the belt brightness, within an  $0.5''$  radius aperture. These flux ratios hint at the source being cold dust. Assuming a standard -3.65 size distribution slope with a minimum grain size of 1  $\mu\text{m}$ , we estimate an emission surface area ( $4\pi r^2$ ) of  $\approx 6 \times 10^{19} \text{ m}^2$  for the dust within the cloud (mass of  $1.36 \times 10^{-7} M_{\text{Earth}}$  up to 1 mm radius grains assuming 2.7 g cm $^{-3}$  bulk density). This is an order of magnitude more dust than we estimated for the scattering surface for Fomalhaut b ([Gáspár and Rieke, 2020](#)). A catastrophic collision between two objects of 355 km radius at a velocity of 360 m s $^{-1}$  (which corresponds to  $\sim 10\%$  of the orbital velocity at the GDC’s location) would be able to produce the amount of dust observed, based on

collisional calculations using equations in [Gáspár et al \(2012\)](#). Alternatively, chance alignment with a background source is not ruled out by this single epoch observation.

### 2.4 Fomalhaut b

Fomalhaut b, along with the planets of HR 8799, were the first directly imaged extrasolar planet candidates orbiting a star ([Kalas et al, 2008](#); [Marois et al, 2008](#)), although the status of Fomalhaut b was always contentious due to non-detection at near-infrared wavelengths ([Kalas et al, 2008](#); [Janson et al, 2012](#)). There have been various hypotheses explaining the nature of the object, including scattered light from a circumplanetary disk ([Kennedy and Wyatt, 2011](#); [Kenyon and Bromley, 2015](#)) or a giant impact between two larger planetesimals ([Galicher et al, 2013](#); [Kenyon et al, 2014](#); [Lawler et al, 2015](#)). [Gáspár and Rieke \(2020\)](#) showed that the HST observations reveal the object to have faded over the decade of observations as well as broadened in size, indicative of an expanding dust cloud. The object is moving on an escape trajectory, pointing to these dust particles being small in size with motions dominated by stellar radiation pressure, indicating they were created in a recent massive collision.

Based on models presented in [Gáspár and Rieke \(2020\)](#), the object should be at  $\Delta\alpha \approx -9''.809$  and  $\Delta\delta \approx 11''.665$  on its unbound orbit (or at  $-9''.377, 11''.144$  if on a bound orbit) at the time of the JWST observations. We estimate the flux from this object using the best fitting expanding dust cloud model evolved to our observing date ([Gáspár and Rieke, 2020](#)). The estimated surface brightness is  $\approx 0.5$  MJy sr $^{-1}$  at 25.5  $\mu\text{m}$ , which is well within the  $1\sigma$  brightness variation at a radial distance of  $\sim 15''.2$  (see Supplementary Figure 11). Consistent with this estimate, we do not detect any observable signature at either of the coordinates in the imaging at 25.5  $\mu\text{m}$  (the region was not imaged at the other wavelengths).

A lingering concern for the collisional hypothesis was the lack of disk material observed interior to the KBA ring, indicating a quiescent and low planetesimal density at the point of origin for Fomalhaut b. Our JWST observations, however, reveal that this location – the intermediate belt – has high dust density. The asymmetric nature of

the belt also hints at increased collisional activity in the region. The JWST observations therefore address the concerns about the expanding cloud hypothesis.

### 3 Discussion

The cold KBA debris belts are often well resolved, particularly with ALMA (e.g., MacGregor et al., 2013; Ricci et al., 2015; MacGregor et al., 2017; Faramaz et al., 2021). Planetary systems will likely lie within these belts. The gravitational fields of planets will carve structures in any interior debris components; the placement of these components gives clues to the existence and architecture of exoplanetary systems. Until now, these clues have not been accessible: (1) infrared SEDs indicate the presence of interior disk components but cannot reveal their structure well; and (2) imaging scattered light in the visible and submm emission with ALMA have not even achieved solid detections in these regions.

This problem has been abolished with MIRI on JWST, which combines the necessary resolution, sensitivity to low surface brightness, and an array of useful tools (multiple imaging filters, coronagraphs, integral field unit spectroscopy). We have turned this revolutionary capability onto the best-resolved bright debris system, that around Fomalhaut. The results have not disappointed. We have detected the dust being blown out of the KBA ring, and in addition have found (1) a narrow intermediate debris belt interior to the KBA ring, (2) a diffuse distribution of dust in a disk-like configuration closer to the star, and (3) a possible dust cloud located within the KBA ring itself (this source being a background object is not currently ruled out). The intermediate belt also reveals increased dust production and collisional activity at the location assumed for the origin of the object Fomalhaut b, supporting the hypothesis that it was produced in a massive collision.

In addition, the structure of the inner debris indicates that it is shepherded through the gravitational influence of yet unseen planets. Planets as low in mass as Neptune are sufficient to carve the inner belts. That is, our observations provide insights to the Fomalhaut planetary system extending down to common planet masses. The structures of the massive debris belts, their alignment offsets, and the indications of massive

collisional events (Fomalhaut b and the GDC) all highlight that the 440 Myr old star Fomalhaut is surrounded by a complex planetary system undergoing dynamical perturbations.

### 4 Methods

We describe the JWST/MIRI observations and detail the reduction steps of the 25.5  $\mu\text{m}$  F2550W dataset in this section. Similar information about the coronagraphic 15.5 and 23.0  $\mu\text{m}$  JWST/MIRI and optical wavelength HST/STIS observations can be found in Supplementary Information section 1. We show our final reduced and processed F2550W image of the Fomalhaut system in Supplementary Figure 1.

The MIRI wavelengths we observed (15.5, 23.0, and 25.5  $\mu\text{m}$ ) equate to the peaks of blackbodies with temperatures of 186, 125, and 113 K, respectively. Assuming 10  $\mu\text{m}$  radius classic astro-silicates (Draine and Lee, 1984), these temperatures correspond to distances of 7.1 au (0''.9), 15.7 au (2''.0), and 19.3 au (2''.5) at Fomalhaut, respectively. The thermally equivalent distances in the Solar System are 1.8, 3.9, and 5.0 au, i.e. regions extending from the orbit of Mars to that of Jupiter. These angular separations are readily resolved at 15.5  $\mu\text{m}$  with the 4QPM and at 25.5  $\mu\text{m}$  via non-coronagraphic imaging with MIRI. In addition, colder ( $\sim 50$  K) dust, located for example in the KBA regions, will still emit  $\approx 20\%$  of its peak flux at 25.5  $\mu\text{m}$  and was therefore also expected to be detected in the observations.

#### 4.1 JWST Observations

Our Cycle 1 GTO observations (PID 1193) were carried out on October 22, 2022, for both MIRI (Wright et al., in press) and NIRCam (Rieke et al., 2023b), using a continuous non-interruptable sequence. The observing program is a result of a collaboration between the MIRI and NIRCam GTO teams, who joined efforts on the same targets (Fomalhaut, Vega, and  $\epsilon$  Eridani). The MIRI program focused on observations at longer wavelengths to reveal the inner disk structure, while the NIRCam observations were designed to detect extrasolar planets. This paper discusses the MIRI observations only. Without prior knowledge of the structure of the ABA disk, we designed the observations to probe various regions in the system.

We therefore included high-contrast imaging via coronagraphy at 15.5 and 23.0  $\mu\text{m}$  and reference differential imaging (RDI) via non-coronagraphic imaging at 25.5  $\mu\text{m}$ . The latter took advantage of the remarkably stable telescope Point Spread Function (PSF).

Reference PSF observations were taken at each wavelength contemporaneously with the science target data acquisition as well as background measurements for the MIRI coronagraphic observations. Apart from a single guide star failure for our MIRI F2550W imaging visit to the PSF reference source, which was repeated on November 13, 2022, our imaging sequence was successfully executed. We summarize the complete set of JWST/MIRI observations in Supplementary Table 1, in the sequence they were carried out. The MIRI+NIRCam sequence was optimized for various aspects of our observing goals and also to save observatory (slewing) overheads. The MIRI sequence was specifically designed to provide long downtimes between using the same detector locations to avoid latent images. For PSF reference, we observed 19 PsA (M3III) at all wavelengths, which proved to be an excellent choice. Although 19 PsA is 100x fainter than Fomalhaut in the V band, it is 10-15% brighter than Fomalhaut at the MIRI wavelengths and its photospheric emission across the MIRI bands mostly follows a Rayleigh-Jeans function, providing a close match to the spectrum of Fomalhaut. 19 PsA is also located at an offset of only 3.3°, providing similar background characteristics as well as ensuring very little thermal variation in the telescope optics.

The target observations were obtained at two rotation angles, offset by 10 degrees, to provide rotational coverage and dithering. The coronagraphic PSF observations were obtained on a 9pt small grid dither (SGD) pattern, which ensured a well-matched PSF. The SGD is especially important for the four quadrant phase mask (4QPM) observations at 15.5  $\mu\text{m}$  (and as we learned less important for the Lyot at 23.0  $\mu\text{m}$ ; Supplementary Information section 1.2). Having a brightness matched PSF reference ensured similar noise characteristics as for the target, which was especially important for the F1550C observations, where only the two closest matching dither position observations of the 9 point small-grid-dither pattern were used in our classical reference differential

imaging reductions. The non-coronagraphic observations with the F2550W filter were also spatially dithered in a larger “extended” source pattern at 4 pointing positions to correct for latent images and uneven background subtractions. Additional details about the individual observations can be found in the following subsections and in Supplementary Information section 1.

## 4.2 MIRI 25.5 $\mu\text{m}$ imaging and processing

Fomalhaut itself is quite bright even at these wavelengths ( $\sim 2.52$  Jy), therefore we had to mitigate the effects of saturation and latent images. While the standard full imager integration time is 2.775 seconds per group (aka frame), shorter integrations are available in subarray modes. We used the Brightsky subarray for the non-coronagraphic imaging program, which reads out a smaller  $512 \times 512$  array with only 0.865 s integrations. These shorter frame times ensured that only a handful of pixels saturated in the stellar core, while we were still able to record 5 frames per integration. The 56'' field of view (FOV) of the Brightsky subarray also ensured that the entire Fomalhaut disk was within the imaged area, even using the larger extended source dither pattern, at any possible orientation. The extended source dither pattern enabled us to construct an even background and further mitigated the effects of imager saturation and detector/background artifacts.

The data were downloaded from the Mikulski Archive for Space Telescopes (MAST), which archives the observations at all processing stages. For the reductions of the F2550W images, we used the raw uncalibrated images (`_uncal.fits`) and reduced them with the pipeline (v. 1.8.2) to stage 2. In general, these steps involve detector-level corrections, ramp-fitting, observing-mode corrections, and calibrations. We turned off dark corrections for the reduction steps, as the background images we later generated using the reference PSF observations included the same dark patterns, given we employed an identical observing sequence for the reference source. These stage 2 products (`_cal.fits` files) still contain detector-level artifacts for MIRI, typically varying background levels, row and column effects, saturation columns and slewing tracks (in our particular case), and

the “tree-ring” structure (Ressler et al, 2008). Further image reductions to remove these artifacts, as well as the image processing steps, were performed using IRAF. The “tree-ring” was removed with a background correction image, produced by median combining the PSF images (19 PsA) without any alignment. Even with the extended dither pattern the stellar contribution was not removed completely with an initial median combination. We corrected this, by generating a median combined PSF, which was then removed from individual images prior to merging them. This process was repeated iteratively, with the generated background also removed from the individual images at each step. The background image produced after five iterations was used to correct the Fomalhaut and the reference PSF images. We removed the remaining row effects by median averaging the rows and subtracting these values from the images, while the constant background level was set to zero by an iterative  $3\sigma$  clipped median sky subtraction. These steps were executed on both the target and reference observations at each dither position independently. We did not execute the stage 3 processing on the dataset; therefore, geometric distortion corrections were not applied to the images we present in this work, but are estimated to be less than 1.5 px over the  $\sim 18''$  extent of the Fomalhaut disk (< 0.9% over the entire detector; Bouchet et al, 2015).

Our Fomalhaut data are the first PSF reference subtracted high SNR observations of any object with JWST at these wavelengths, therefore no standard reduction steps have been developed. To determine the ideal processing steps, we tested multiple methods with the dataset. As the initial PSF reference observations failed at 25.5  $\mu\text{m}$ , we first reduced the dataset using theoretical PSFs and a lower-quality noisier observed PSF ( $\beta$  Dor; PID 1023) obtained during commissioning, and also via angular differential imaging (ADI) techniques, while waiting for the repeat PSF observations. The theoretical PSF, generated using WebbPSF (Perrin et al, 2014) and employing the contemporaneous optical path difference (OPD) information of the observatory, proved to be insufficient for our purposes, revealing significant differences in scaling and patterns between the observed and modeled PSF structures. The variances are likely to arise predominantly due to the brighter-fatter-effect in the MIRI detectors

(I. Argyriou et al. 2023, in preparation), which is not included in the WebbPSF simulations. Efforts to improve on the theoretical PSF proved to be fruitless. The PSF observed during commissioning provided a much better subtraction of the stellar core, but has a much lower SNR and therefore introduced noise levels greater than the disk signal we were seeking to reveal even near the core. Additionally, these observations used the SUB256 subarray, which has a smaller FOV of only  $28''$  (smaller than the full extent of the Fomalhaut KBA ring at  $38''$ ), thereby disqualifying this PSF to be used in reducing the entire FOV.

However, some interesting discoveries were made about the JWST Optical Telescope Assembly (OTA) and MIRI optical system when we performed classical ADI reductions. The two Fomalhaut F2550W observations, offset by  $10^\circ$  in position angle, were separated by 10 hours, to allow the detector to erase latent artifacts without annealing. Assuming minor temporal variations in the optical system, as an initial attempt we combined all Fomalhaut target observations to produce a “super” PSF and used this as a reference to subtract. This method resulted in an image with expected self-subtraction residuals due to the extended disk signal, and only marginally better results within the PSF core than what we achieved using the theoretical PSF. As a second method, we subtracted only the matching dither position pairs from each other. These subtractions resulted in virtually zero residuals of stellar contribution, even with the 10 hour gap between their acquisition (with the disk self-subtractions obviously still present). This result is true at all four dither positions. The MIRI PSF – at least at these wavelengths – is remarkably stable but position dependent (at the levels revealed by precise PSF subtraction).

The stability and position dependence of the PSFs were corroborated with the repeat observation of our PSF target at 25.5  $\mu\text{m}$ , which provided residual-free subtractions, as long as PSFs obtained at the same detector locations were used. To highlight the position dependence of the PSFs, we show their differences relative to each other (the same reference source - 19 PsA - subtracted from itself) in Supplementary Figure 2. The residuals are on the level of the disk signal we are detecting. To demonstrate the position dependence of the PSFs and accurate matching when

using the same position, we show the PSF subtraction residuals for Fomalhaut at the first dither position in Supplementary Figure 3. When using the PSF obtained at the same detector position (D1), there are no detectable residuals, while the PSFs obtained at positions 2 and 3 yield noticeable patterns. The PSF imaged at D4 is better, but still shows some residuals. Subtractions of the target images taken at D2, D3, and D4 yielded similar results. The residuals are speckle-like in pattern and are not a result of the uncorrected geometric distortions.

Although the PSF reference observations were executed three weeks after the target observations, due to their initial failure, the subtractions again showed no detectable stellar residuals, as long as the PSFs were subtracted in pairs corresponding to the same detector positions. Our PSF target, 19 PsA, is slightly brighter than Fomalhaut at  $25.5\text{ }\mu\text{m}$  (2.88 vs. 2.52 Jy) and we obtained identical exposures for it as we did for Fomalhaut, thereby guaranteeing matching PSFs. We achieved residual-free subtractions using a PSF scaling factor of 0.9; at 0.87 and 0.93 under- and over-subtraction residuals were apparent. Following masking for latent patterns, individually for each of the eight images, we median combined the dataset with  $3\sigma$  clipping around the data median.

We derived the absolute calibration from the reference star. For MIRI, the minimum number of frames per ramp is 5 to ensure a well sampled integration slope. The first and last frames of a ramp are not used, therefore, the slopes only consisted of 3 frames for analysis purposes. The current pipeline does not apply a reset switch charge decay (RSCD) correction (Morrison et al., in prep) for such short ramps, therefore the absolute calibration of the  $25.5\text{ }\mu\text{m}$  images was uncertain. To verify the absolute calibration, we used the observations of the PSF target, 19 PsA, which were carried out in an identical way to the target observations, therefore should be subject to the same systematic offsets. The reference observations were of a clean point source, allowing us to compare it to a theoretical PSF. While the particular speckle pattern of the theoretical PSF is not an ideal match, as shown previously, we can use it globally for photometric calibration. For this purpose, we used the theoretical PSF that we generated for our initial reductions, using the available OPD maps of the telescope. While

the reference observations were taken three weeks after the target observations, we were informed by the Space Telescope Institute that the optical maps were identical for the purposes of modeling the  $25.5\text{ }\mu\text{m}$  PSF (Marshall Perrin and Matthew Lallo, private communication). This was corroborated by the clean PSF subtractions shown in Supplementary Figure 3. We confirmed that the core of the theoretical PSF agrees with the observations, by making a comparison to the  $\beta$  Dor observations previously introduced. In Supplementary Figure 4, we show the radial profile of the observed PSFs and the fitted theoretical one, where we apply a radial location dependent scaling function to the latter. The radial-dependent scaling function was necessary to obtain a better fit at radial offsets greater than  $10''$ , varying linearly from a value of 36.5 at the stellar core to 13.33 at  $20''$ . The total integrated flux of the scaled theoretical PSF is 2580 mJy, while the predicted photospheric brightness of 19 PsA was 2880 mJy. As 19 PsA is a small amplitude (1-2%) variable star, we also used the flux value determined from our fitting to the Fomalhaut observations, where we determined a scaling factor of 0.90 for it to fit the target observations. Fomalhaut has a brightness of  $2570 \pm 50$  mJy at  $25.5\text{ }\mu\text{m}$ , yielding a brightness of  $2855 \pm 55$  for 19 PsA, in excellent agreement. Based on these estimates, we applied a  $1.11 (\pm 0.02)$  scaling factor to the F2550W images for absolute calibration.

**Data Availability.** The final reduced and processed JWST MIRI imaging data that we present in this paper (and ones including geometric distortion corrections) can be downloaded from <https://github.com/merope82/Fomalhaut>. The raw and general pipeline processed data products will be available from the Mikulski Archive for Space Telescopes (MAST) at the Space Telescope Science Institute following their public release. The JWST observations are associated with program #1193, while the HST observations are associated with program 15905.

**Acknowledgments.** We would like to acknowledge the assistance of our program coordinators, Crystal Mannfolk and Blair Porterfield, especially in ensuring a quick repeat of the initially failed PSF reference observations. We want to thank Marshall Perrin and Matthew Lallo for updating us on the primary mirror alignment while we

waited for the repeat of the PSF observations. Financial support for this work was provided by Grants 80NSSC22K1293 and HST-GO-15905.001-A to the University of Arizona. This work is based in part on observations made with the NASA/ESA/CSA JW and Hubble Space Telescope. The data were obtained from the Mikulski Archive for Space Telescopes at the Space Telescope Science Institute, which is operated by the Association of Universities for Research in Astronomy, Inc., under NASA contract NAS 5-03127 for JWST.

**Author Contributions.** The observations were designed by A.G. and G.R., the data were reduced and processed by A.G. and S.W., while all co-authors contributed to the data analysis and writing of the manuscript.

**Competing Interests.** The authors do not declare any competing interests.

# Supplementary information

## 1 Observations - continued

**Supplementary Table 1** JWST MIRI observations of the Fomalhaut system (Oct 22, 2022)

Target	Filter	PA <sup>‡</sup>	N <sub>group</sub>	N <sub>int</sub>	Dither	Time (s)
19 PsA (PSF Ref.)*	F2550W	59.20	5	52	4pt Ext <sup>†</sup>	1076.4
19 PsA (PSF Ref.)	F2300C	59.20	95	7	9pt SGD	1956.6
PSF background	F2300C	59.22	95	7	None	217.4
19 PsA (PSF Ref.)	F1550C	59.22	168	5	9pt SGD	1820.6
PSF background	F1550C	59.25	168	5	None	202.3
Fomalhaut (Rot 1)	F2550W	50.65	5	52	4pt Ext <sup>†</sup>	1076.4
Fomalhaut (Rot 1)	F2300C	50.65	102	29	None	967.5
Fomalhaut background	F2300C	56.02	102	29	None	967.5
Fomalhaut (Rot 1)	F1550C	52.06	211	18	None	914.4
Fomalhaut background	F1550C	56.07	211	18	None	914.4
Fomalhaut (Rot 2)	F1550C	62.05	211	18	None	914.4
Fomalhaut (Rot 2)	F2300C	60.63	102	29	None	967.5
Fomalhaut (Rot 2)	F2550W	60.63	5	52	4pt Ext <sup>†</sup>	1076.4

The table reflects the observing sequence we employed to obtain the dataset, which was optimized to reduce latent images in the MIRI detectors, providing long gaps between observations performed at the same detector location/wavelength.

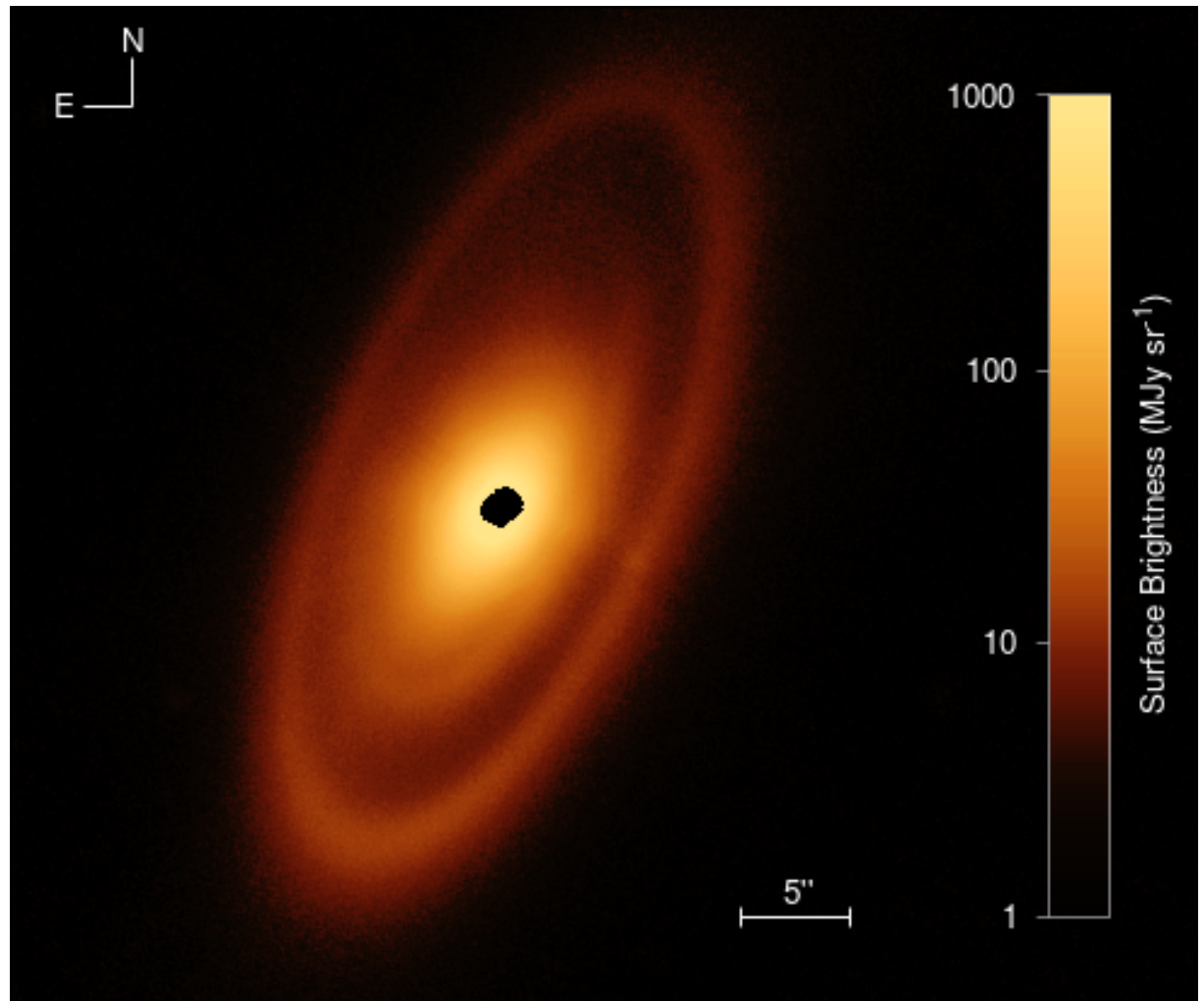
\*This observation failed in the initial sequence due to guide star failure and was repeated on Nov 13, 2022.

<sup>†</sup>The Brightsky subarray 4 pt extended dither pattern used the #6 starting set with a single set.

<sup>‡</sup>Position angle of observed aperture.

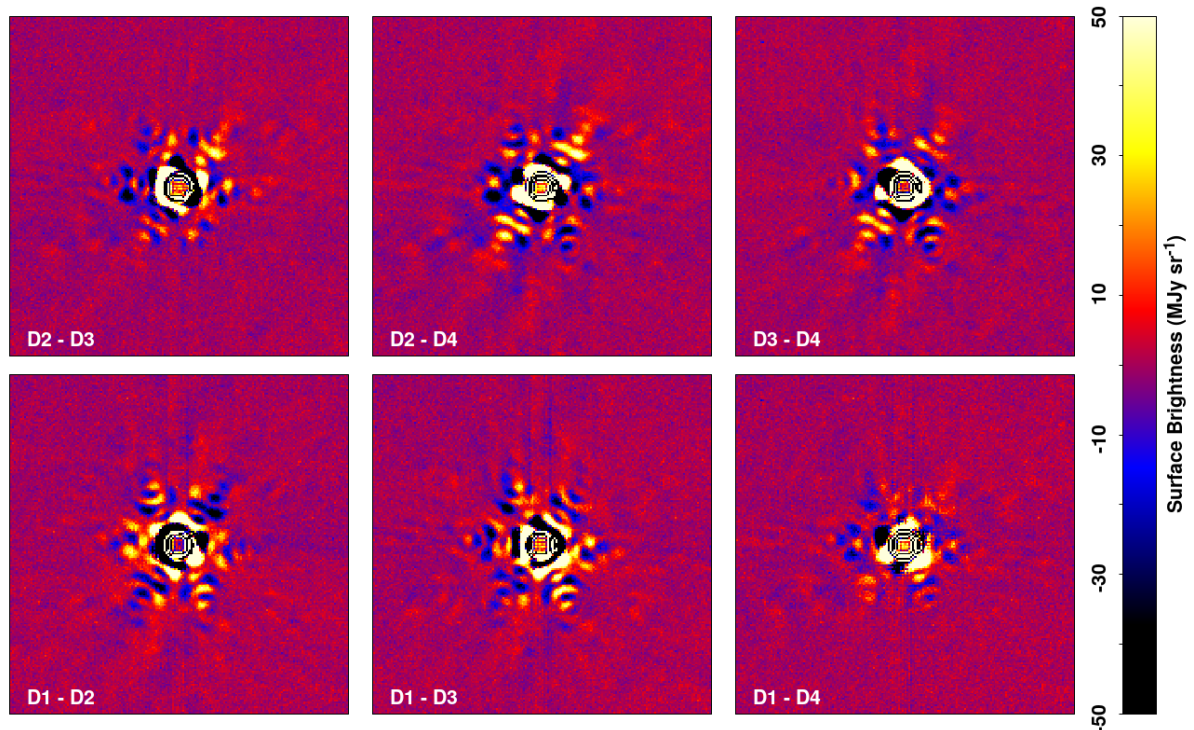
### 1.1 JWST/MIRI 25.5 $\mu$ m imaging extra Figures and Tables

The JWST/MIRI F2550W 25.5  $\mu\text{m}$  non-coronagraphic image of the Fomalhaut debris disk system



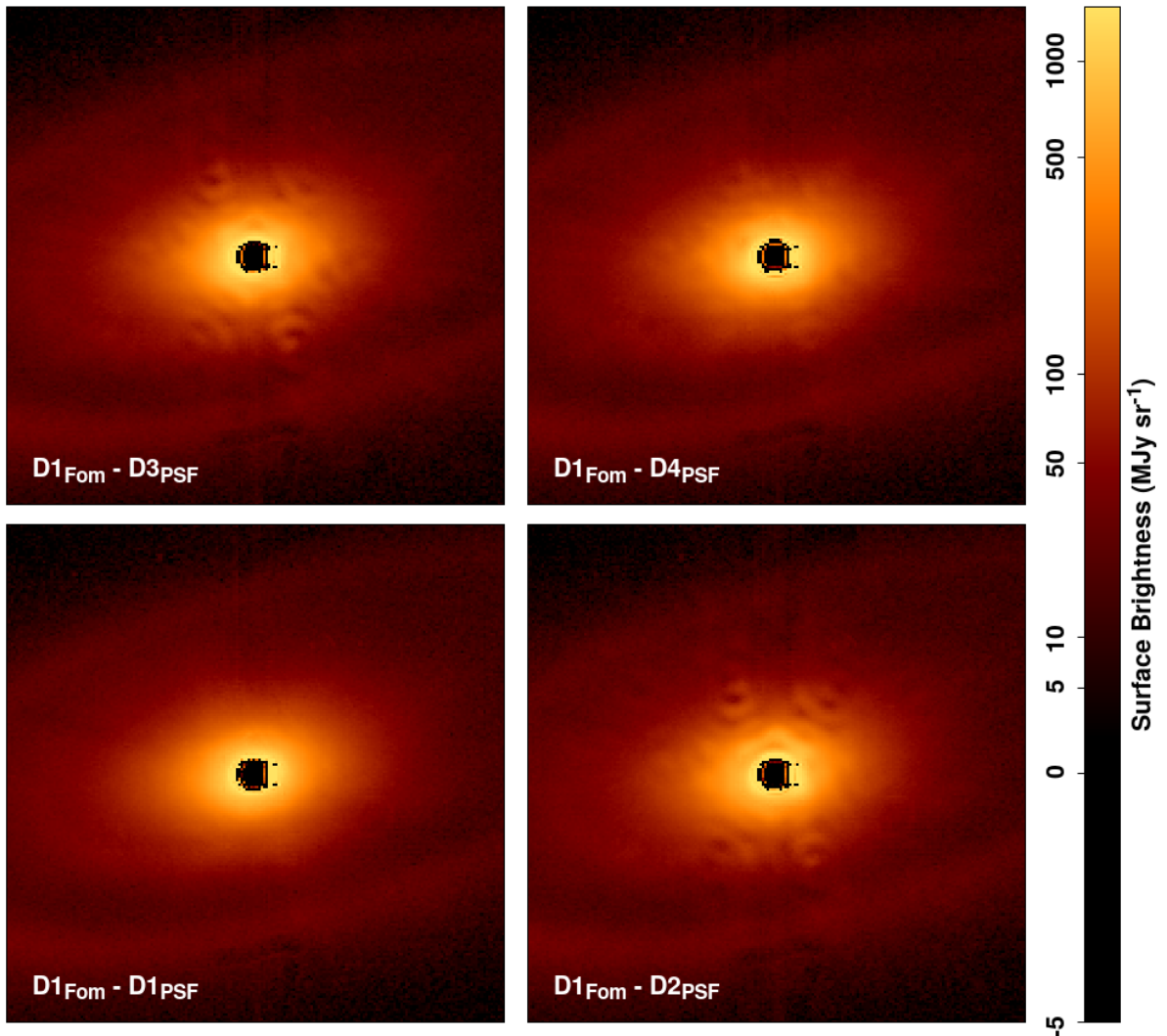
**Supplementary Figure 1** The image, produced via classic reference PSF subtraction, is displayed in logarithmic scaling between -4.6 and 2000 MJy sr $^{-1}$ , with the colorbar showing (part of) the mapping.

Variations of the reference PSF (19 PsA) as a function of detector position in the F2550W images.



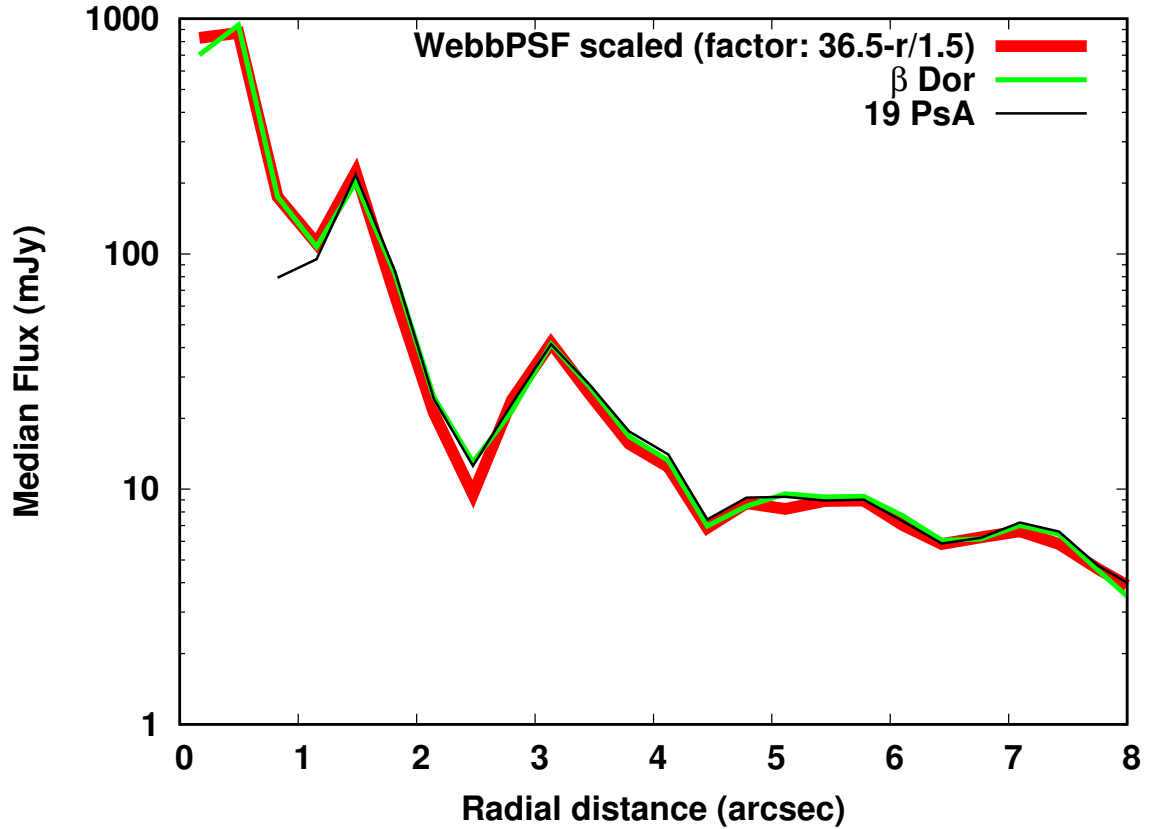
**Supplementary Figure 2** We show all possible subtraction combinations of the 4 dither positions (D1 to D4). The postage-stamp images ( $22'' \times 22''$ ) are scaled between  $-50$  and  $+50$   $\text{MJy sr}^{-1}$ , which is similar to the disk signal level at these locations. Fortunately, the PSFs taken at identical positions remained remarkably stable and could be used for the precise removal of stellar flux (see Supplementary Figure 3).

Test PSF subtractions of the Fomalhaut image at  $25.5 \mu\text{m}$



**Supplementary Figure 3** The test images show the PSF subtractions at the first dither position, using the reference PSF observed at each of the four positions (offset from each other on the order of  $\sim 150 \text{ px}$ ). The figure demonstrates the position dependence of the observed PSF and also how well the matched position PSF is able to remove the stellar contribution. We ended up using only matching position PSFs for the image reductions. The image scaling is logarithmic between -5 and  $1500 \text{ MJy sr}^{-1}$  and the image FOV is  $22'' \times 22''$ . The images are oriented in the observed V3 frame of the observatory.

The observed median radial profile of 19 PsA and the scaled theoretical WebbPSF model.



**Supplementary Figure 4** A radial distance dependent scaling was applied to the theoretical PSF to obtain a better fit at larger distances. The core of the theoretical PSF is verified with the  $\beta$  Dor observed PSF. The total integrated flux of the theoretical PSF was only  $\sim 10\%$  fainter than the photospheric estimate for 19 PsA at  $25.5 \mu\text{m}$ , providing the scaling factor necessary for the absolute calibration of the observations. Importantly, the brighter-fatter-effect that causes differences between the theoretical and observed PSFs preserves charge, so the total flux should be a valid measure.

## 1.2 JWST/MIRI 23.0 $\mu\text{m}$ coronagraphy

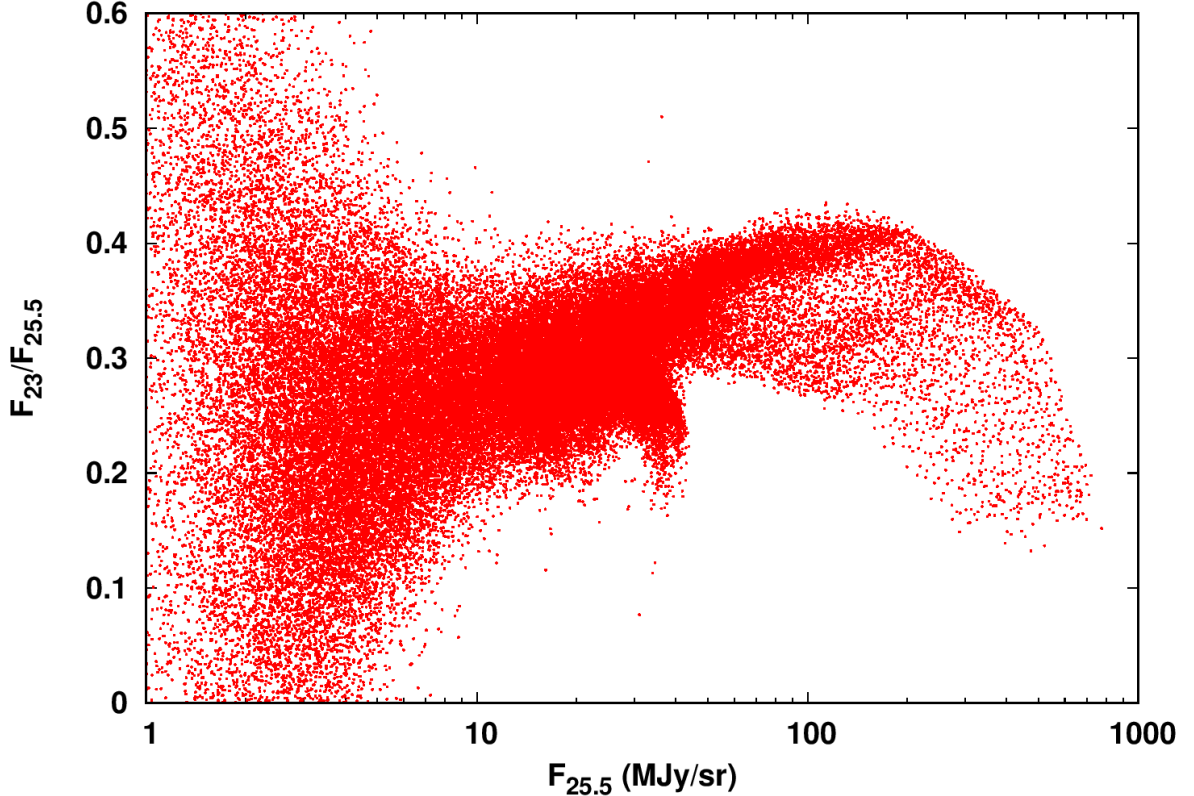
The 23.0  $\mu\text{m}$  coronagraph of MIRI uses a classic Lyot mask to achieve high contrast imaging near bright sources. The mask is rather large, providing an inner working angle (IWA) of  $\sim 3.3\lambda/D$ , i.e.,  $\sim 2''.4$  (Boccaletti et al, 2015). Our data is the first complete reference PSF subtracted set of observations taken with JWST using this mode. Boccaletti et al (2022) present raw contrasts for the F2300C coronagraph showing levels of  $\sim 10^{-3}$  near the IWA and estimates of  $10^{-4}$  when using reference PSF subtraction based on exposure time calculator (ETC) simulations.

The MIRI coronagraphic fields present a scattering artifact along the Lyot mask boundaries – as well as along the 4QPM mask boundaries – known as “glowsticks” (Boccaletti et al, 2022), which are effectively removed via background subtractions. Unlike for the non-coronagraphic imaging at 25.5  $\mu\text{m}$ , dedicated background observations were taken for both Lyot and 4QPM coronagraphic imaging modes. The current status of the JWST pipeline, particularly the mitigation of the “glowsticks”, results in additional noise because of the lack of satisfactory dark frames. Therefore, we processed the science, reference, and background datasets only through stage 2 of the pipeline, producing the calibrated dataproducts (`_calints.fits`). To use the background observations as dark corrections simultaneously, we disabled the internal dark correction in stage 1 of the pipeline. Our background observations for the F2300C dataset were relatively clear of artifacts. We opted to work with the 3D calibrated data products (which include each individual integration), instead of the 2D ones (which combine the integrations), as we gained a bit further flexibility in processing. We median combined the individual integrations within the `_calint.fits` files for the target, reference, and background observations, using a  $3\sigma$  clipping algorithm centered on the data median.

Given the remarkable stability of the longer wavelength PSFs and the Lyot coronagraph’s insensitivity to minor positional offsets, we only perform classical PSF subtraction image processing for this observing mode, using IRAF. We first investigated how well each individual reference PSF subtracted the stellar contribution from Fomalhaut by eye. The SGD of the reference PSF displaces the source in a  $3\times 3$  grid with 10 mas (0.09 px) steps centered on the assumed position of the highest attenuation of the Lyot mask. The coronagraphic target acquisition is precise to 5 mas (0.045 px) (Boccaletti et al, 2022; Rigby et al, 2022), therefore it is highly likely that at least one of the SGD reference observations is close to identical to the science target. This high precision matching is less important for the Lyot mask than it is for the 4QPM coronagraphs, where the PSF structures are highly sensitive to positional offsets. The Lyot PSF is practically identical within the coronagraphic pointing accuracy of the observatory and SGD may not be necessary for observations within this mode. To increase the signal-to-noise ratio of the final product, we include all observed PSFs in our image processing steps, not just the best centered one. Determining the  $\sim 0.05$  pixel offsets between the science and reference frames was complex, requiring us to track the position of the central light peak, a result of either light leaking through the Lyot mask or a diffraction artifact. The scaling for the reference PSF was set to a factor of 0.87, which resulted visually in the least amount of subtraction residuals. Subtraction artifacts started to become apparent at scaling factors of 0.82 and 0.92. Given the large occulted inner region and the high luminosity of the disk at this wavelength, relative to the star, this large range of acceptable PSF scalings is not surprising.

Our 23.0  $\mu\text{m}$  images presented a brightness dependent scaling offset in flux values relative to the 25.5  $\mu\text{m}$  observations, where the images overlapped. In Supplementary Figure 5, we show the F2300C/F2550W flux ratio, as a function of the F2550W brightness, on a per pixel basis. Given the similar wavelengths of the two observations, this was unexpected. The increase in the 23.0 to 25.5  $\mu\text{m}$  flux ratio as a function of brightness could be due to issues with linearity correction, but the global scaling offset points to suspected issues with the pipeline (v. 1.8.2) calibrations at 23.0  $\mu\text{m}$ . This is supported by the fact that we were able to verify the flux calibration of the 25.5  $\mu\text{m}$  data to within 10%. For our current work, we calibrated the F2300C images with the F2550W observations. Based on IRS spectra (see Section “The Asteroid-belt analog”) the inner disk should be around  $\sim 6\%$  brighter at 25.5  $\mu\text{m}$  than at 23  $\mu\text{m}$ . In the colder parts of the disk the ratio is likely somewhat higher. The average  $F_{23}/F_{25.5} = 0.32$  in regions where the F2550W

## The $F_{23}/F_{25.5}$ flux ratio as a function of $25.5\mu\text{m}$ brightness



**Supplementary Figure 5** The  $F_{23}/F_{25.5}$  flux ratio is shown on a per-pixel basis, in overlapping image regions. We would anticipate a flat line near 0.9-1, given Spitzer IRS observations of the system (see Section “The Asteroid-belt analog”) and the near identical observational wavelengths.

flux is between 10 and 100 MJy  $\text{sr}^{-1}$ . To calibrate the  $23.0\mu\text{m}$  data, we multiply the observations by a factor of 3.14. We note therefore that the absolute calibration of the F2300C observations is uncertain.

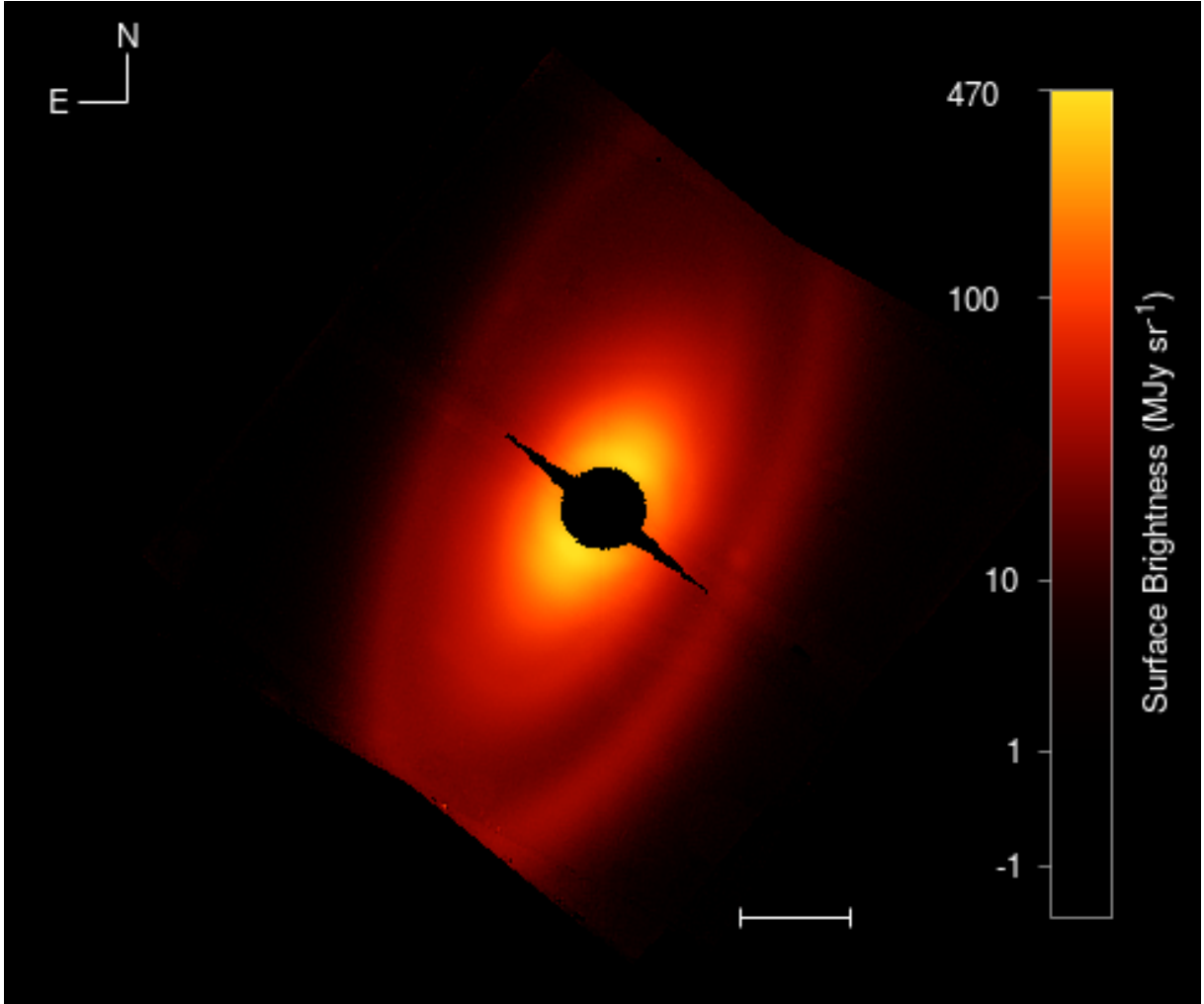
Our final image processing result for the Fomalhaut debris disk system at  $23\mu\text{m}$  is shown in Supplementary Figure 6. The features present in the F2550W image can be identified in the F2300C image as well. While the IWA is larger for the F2300C image, its integration ramps used 102 frames (groups), thereby contributing less noise than the F2550W image from ramp fitting alone.

### 1.2.1 JWST/MIRI 15.5 $\mu\text{m}$ coronagraphy

The  $15.5\mu\text{m}$  coronagraphic mode of MIRI uses a four-quadrant binary phase mask  $(0, \pi)$  to suppress the stellar contribution to the observed signal (4QPM; [Rouan et al. 2000](#); [Boccaletti et al. 2004, 2015](#)). The on-sky performance of the coronagraph has been excellent ([Boccaletti et al. 2022](#)), achieving contrasts of  $\approx 10^{-4}$  within  $1''$ , following post-processing.

Our image reduction steps for these images, up to stage 2, were identical to those used for the Lyot images; i.e. we turned off dark subtractions and processed the images through the standard JWST pipeline otherwise. We did not, however, follow the standard steps for the background subtractions for the F1550C 4QPM observations. Our background images for both the target and reference source did not employ dithers and were contaminated with bright PSF structures from sources outside the FOV. We obtained cleaner background data from the archive, utilizing observations taken within the early release

The JWST/MIRI F2300C 23.0  $\mu\text{m}$  Lyot coronagraphic observations of the Fomalhaut debris disk system.

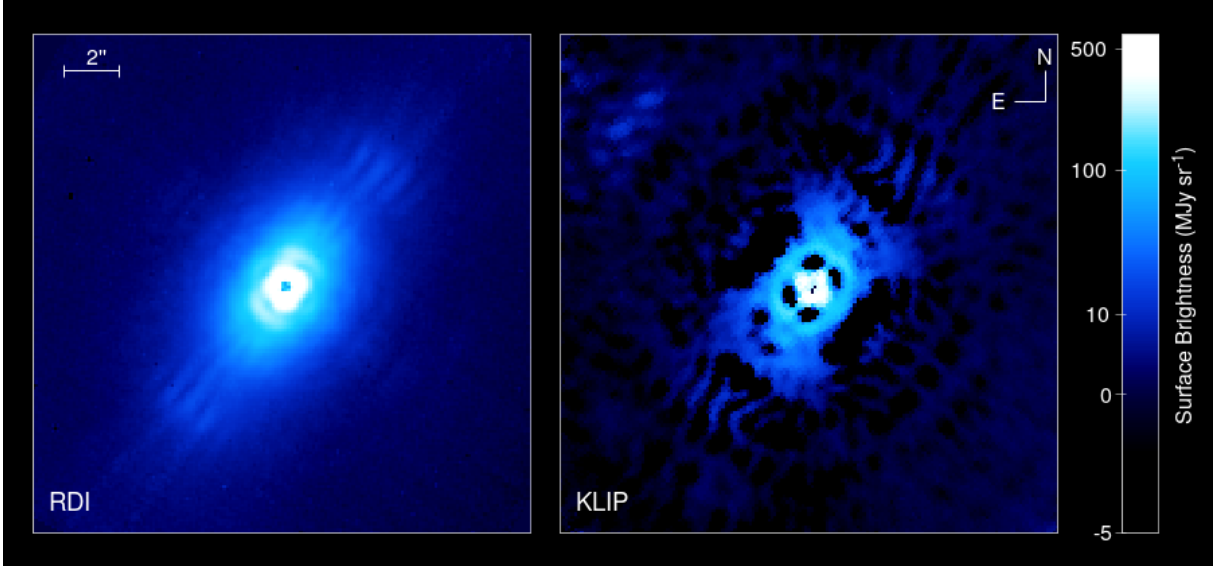


**Supplementary Figure 6** The image is displayed in logarithmic scaling between  $-1.5$  and  $470 \text{ MJy sr}^{-1}$ . The intermediate belt and the secondary gap, previously identified in the F2550W image, are also present in the F2300C image, as well as the extended inner disk.

science program PID 1386 (observations 30, 36, and 37). These observations integrated to larger group numbers than our observations, therefore we truncated them at the same levels as ours to provide similar dark noise characteristics. We also utilized flat-field observations taken in commissioning program PID 1045 (observation 66), using them as background data, for our PSF reference observation. This particular dataset yielded a background image that agreed better with our original PSF background observation, as determined by examining residuals. Background level offsets were determined and corrected using median pixel values in matching clear areas. While the final reduction using the archival background images contained less artifacts, it is characteristically and photometrically identical to the version using the dedicated background observations. Following the removal of the background from the 2D PSF and Fomalhaut images, the “glowsticks” were effectively removed.

[Boccaletti et al \(2022\)](#) show that classic RDI yields comparable results to the Karhunen-Loeve Image Processing algorithm (KLIP; [Soummer et al, 2012](#)) at  $15.5 \mu\text{m}$ ; therefore, our team processed the coronagraphic observations using both classical Reference Differential Imaging (RDI) as well as Principal

The JWST/MIRI F1550C 15.5  $\mu\text{m}$  4QPM coronagraphic observations of the inner regions of the Fomalhaut ABA disk.



**Supplementary Figure 7** An asymmetric extended inner disk is detected in the observations, mostly aligned with the outer KBA narrow ring, which is not detected. While our pre-launch models assumed a narrow inclined ring – similar to the KBA ring – the observations show that the inner ABA region of Fomalhaut is rather extended and has low surface brightness. Unfortunately, our observations were oriented such that the position angle of the ABA disk aligned with the PSF artifacts of the 4QPM. Image scaling is between -5 and 600 MJy  $\text{sr}^{-1}$ .

Component Analysis (PCA) based on combined reference PSF subtractions employing KLIP. Below, we give a summary of our processing steps using these two different methods. In Supplementary Figure 7 we show the results of the two reduction methods for the 15.5  $\mu\text{m}$  4QPM observations of the Fomalhaut system. We did not pursue ADI image processing, as the 10° rotational dither (the limit the observatory can rotate around its nominal orientation) did not provide adequate offset at such small inner working angles.

First, we describe our classical RDI image processing, all performed using IRAF. Our processing steps were similar to those employed for the F2300C mode, with one notable difference. While we fitted PSF offsets at F2300C, for the 4QPM PSF subtractions we purposely did not apply any positional shifts. As the 4QPM PSF structures are position dependent, shifting the PSFs to obtain a better subtraction is mostly a futile exercise (either the subtraction works without shifts applied or it does not at all). For PSF scaling, we investigated values near the ratio of the photospheric emission of Fomalhaut vs. 19 PsA, which is  $\sim 0.9$  at 15.5  $\mu\text{m}$ . We noticed clear over-subtraction residuals at a factor of 0.92 (for 19 PsA) and under-subtraction at 0.85, therefore settled on the factor of 0.88. The best fitting PSFs (ones with the least residuals following subtractions) were removed from the target observations at both orientations. For the Fomalhaut Obs #9 image we used the PSF taken at SGD position #2 and for the Fomalhaut Obs #11 we used the PSF taken at SGD position #1. Following masking and image derotations, the two images were averaged.

The JWST pipeline has a KLIP implementation included in stage 3 (`calwebb_coron3`), which first performs outlier rejection and determines the reference PSF alignment via least squares. The main limitation of this KLIP variant is the lack of user input; the only parameter the user can define is the number of KL modes to use in the subtraction (the default is 50). For this reason, we also tested the spaceKLIP software developed by the JWST High Contrast ERS team (PI Sasha Hinkley), which is much more interactive and contains built in analysis tools; for more details on spaceKLIP see [Kammerer et al \(2022\)](#) and [Carter et al \(2022\)](#). Ultimately, we found that, for extended disk observations where a single subtraction zone is optimal, spaceKLIP and the JWST pipeline KLIP produce equivalent results. In this work,

**Supplementary Table 2** Multi-roll *HST* coronagraphic observations of the Fomalhaut system at WEDGEA0.6 and WEDGEB0.6

Target	Date	PA orientations ( $^{\circ}$ )	Time	$N_{WA0.6}$	$N_{WB0.6}$
Fomalhaut	Aug-23-2020	-83.61, -86.69, -103.36	27.0 s	$45 \times 3$	$45 \times 3$
Fomalhaut	Nov-18-2020	40.05, 24.45, 10.61	28.5 s	$45 \times 3$	$50 \times 3$
$\Theta$ Peg (PSF)	Nov-18-2020		27.0 s	$45 \times 3$	$45 \times 3$
Fomalhaut	Aug-20-2021	-83.70, -86.57, -103.20	27.0 s	$45 \times 3$	$45 \times 3$
$\Theta$ Peg (PSF)	Aug-20-2021		27.0 s	$45 \times 3$	$45 \times 3$

we elected to use the JWST Pipeline KLIP variant for simplicity, resuming the processing of the images following our custom background subtraction to stage 3. We performed KLIP processing with a single KL mode. For the reference library, we used the entire set of nine SGD images obtained for the reference target.

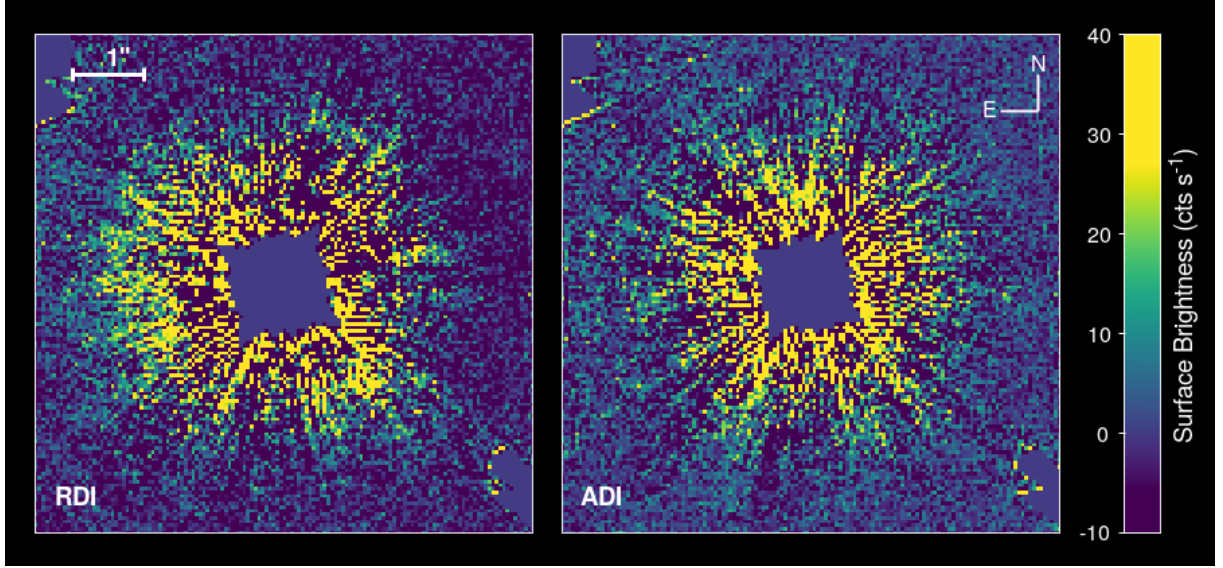
Our tests show that the classical RDI methods yield smoother reductions than KLIP for extended sources observed with the F1550C 4QPM. This is mostly due to the over-subtraction with KLIP (which becomes worse as more KL modes are included), as it is unable to differentiate between stellar and extended brightness features. In our analysis we used our classical RDI processing results.

### 1.3 Cycle 27 HST Observations

We were awarded 8 orbits of HST time in Cycle 27 (GO 15905) to observe the ABA disk around Fomalhaut in scattered light using STIS. Previous coronagraphic observations had a relatively large inner working angle (IWA) due to use of the WEDGE2.5 occulting positions. Our observations were designed to yield a  $360^{\circ}$  image of the inner regions down to IWAs of  $0.^{\prime\prime}3$ . To accomplish this, we used two coronagraphic positions within the same visits (orbits), which were located on the perpendicularly intersecting WedgeA and WedgeB occulting bars. The small IWA was achieved with the standard WedgeA0.6 position and its unofficial pair on the WedgeB bar that is reached by using additional POSTARG commands from the WedgeB1.0 aperture. This observing method has been previously successfully executed by [Apai et al \(2015\)](#) to observe the  $\beta$  Pictoris debris disk (GO 12551). With the two Wedge positions, we achieved adequate rotational dithers and a full roll coverage of the system. Our observations were split into two groups of four, due to scheduling and rotational constraints; therefore, the initial planned dataset consisted of 2 reference and 6 target observations. Unfortunately, the PSF observations failed in the first epoch, therefore the entire first set of observations was repeated. In Supplementary Table 2, we summarize the HST dataset.

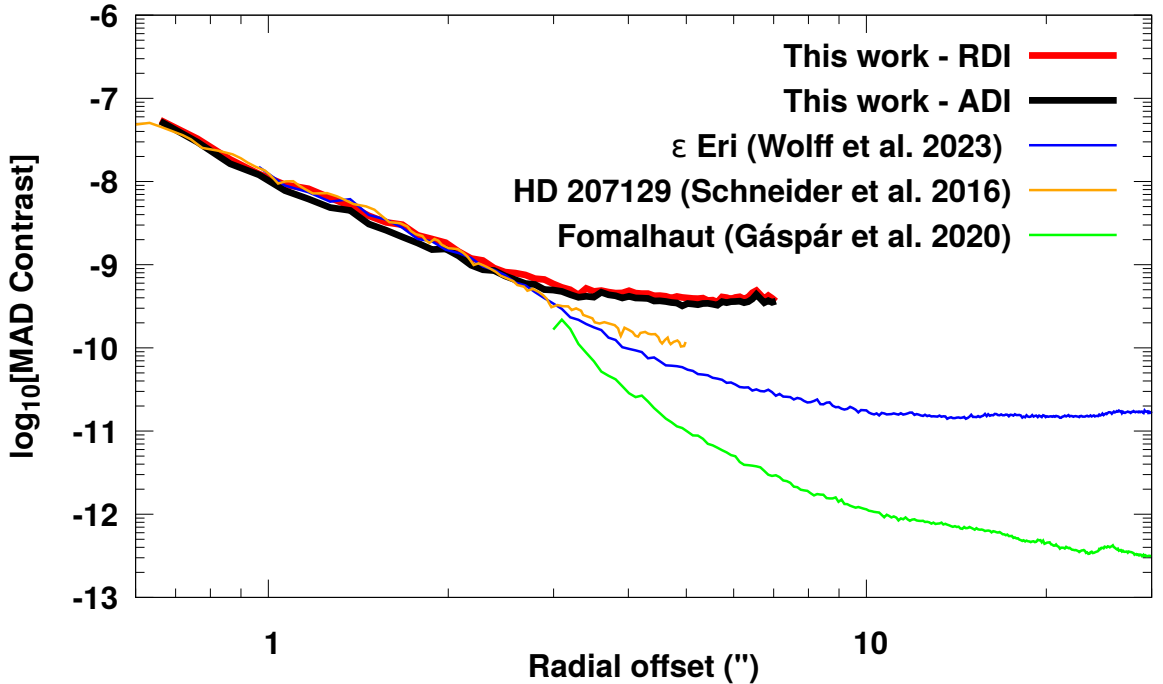
Reductions of the datasets followed along the lines of our  $\epsilon$  Eridani observations ([Wolff et al, 2023](#)), where we first removed the video-noise inherent in the STIS data using the autofillet idl package ([Jansen et al, 2003](#)) and then reduced the corrected raw data with the calstis pipeline. These HST observations were amongst the most challenging, in terms of image processing, ever taken. Since Fomalhaut was near saturation at the WA0.6 aperture, we recorded 820 individual frames of Fomalhaut alone, and 175 of its reference calibrator. To lessen the workload, we first median combined the individual frames in groups of five (in sequential order), thereby having only 164 Fomalhaut frames to individually cross-reference with 35 PSFs. Numerical algorithms are not as accurate as the human eye in finding optimal alignment and scaling between target and reference data; therefore, we first found the best fitting PSF for each observed target observation using an initial best-guess of its center location with centerRadon ([Ren et al, 2019](#)). Once the best matching PSF was found for each target observation, they were individually re-aligned. While on average centerRadon works well, we found small adjustments necessary to achieve ideal subtractions. At WA0.6 our average shifts were  $\Delta x = -0.0177 \pm 0.0321$  and  $\Delta y = 0.00556 \pm 0.0304$  pixels, while at WB0.6 they were  $\Delta x = 0.00569 \pm 0.0566$  and  $\Delta y = -0.0389 \pm 0.0787$  pixels. While these may seem negligible, at 0.05 px offset subtraction speckle residuals are the major source of noise; therefore, this was a necessary step. Finally, we also adjusted the scaling of the PSFs for each matched and aligned combination to produce the same signal level. Following masking, image translations/rotations, and finally combining the images via median averaging (and iterative sigma clipping around the data

The inner regions of the Fomalhaut system with the HST Cycle 27 (GO 15905) observations.



**Supplementary Figure 8** The left panel shows the RDI reduction while the right panel shows the ADI reduction results, using classical PSF subtraction methods. Both images are displayed in linear scaling between  $-10$  and  $40 \text{ cts s}^{-1}$ . The observations/reductions are contrast limited out to  $3''$  and we do not detect any discernible levels of extended scattered light emission at any location.

The Median Absolute Deviation contrast achieved with the HST Cycle 27 (GO 15905) observations.



**Supplementary Figure 9** Given the short total integration time of less than 1.5 minutes - a result of the planned small IWA of the observations - our achieved contrast levels taper off to being photon limited at around  $3''$ .

median), our image processing work resulted in the null detections we show in Supplementary Figure 8. In the figure, we also present a reduction using ADI methods, where we performed the same operations as above, just cross-refencing the Fomalhaut observations with themselves, avoiding the orbits where the orientation angles were within  $10^\circ$  of each other. While the observations totalled only less than 1.5 minutes of integration time on target, the contrast levels we achieved are nonetheless impressive, especially compared to other, much longer integration programs, as shown in Supplementary Figure 9. Our combined dataset is contrast limited to around  $3''$ . Within that region, however, our reductions are on-par with programs using significantly longer integrations, due to the absolute brightness of Fomalhaut and the remarkable stability of the HST optical system. However, these observations cannot compete with the contrast levels achieved in [Gáspár and Rieke \(2020\)](#), which combines over 8 hours of STIS data using much larger coronagraphic apertures (thereby imaging only the outer regions of the system).

The lack of a scattered light detection with HST may seem surprising, given the bright warm component observed in the MIRI data. Our assumption that the component could be observed with HST was based on the spatially unresolved warm excess with Spitzer ([Stapelfeldt et al, 2004](#); [Su et al, 2013](#)). These data hinted at a compact inner disk, one very similar to the Solar System asteroid belt. The JWST images show that the warm component is spatially extended, thereby having a much lower scattered light surface brightness than we expected. The JWST and HST observations together enable complex modeling of the dust grain properties and light scattering functions, which we will address in future papers.

## 2 Analysis: Supplementary Information

### 2.1 Photometry

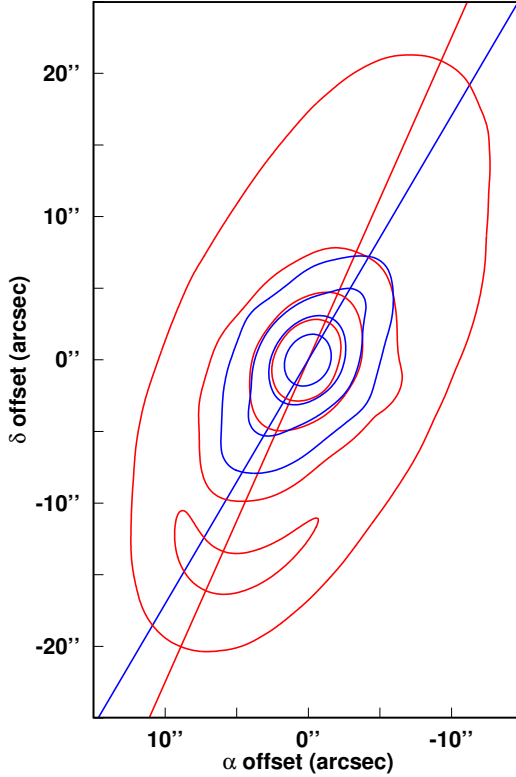
Photometric analysis was performed on the images in two configurations: in the observed frames and also on de-projected images. Photometry in the observed frames allow for comparisons with previous measurements, where the inner regions were not resolved spatially, while photometry of the de-projected images yields the input for modeling the system. Statistical errors were calculated using the error frames of the observations, while systematic errors from PSF fitting were estimated using the scaling ranges we determined with by-eye fitting. At  $25.5$  and  $23.0\ \mu\text{m}$  we also include an additional conservative 5 and 10% systematic error term in quadrature, respectively, to allow for offsets from the absolute calibrations. The allowed error at  $23.0\ \mu\text{m}$  was set to be larger, due to the added uncertainty in the scaling factor from the  $25.5\ \mu\text{m}$  observation. The systematic errors were the dominant error terms at all wavelengths. We assume the systematic error terms of these observations to improve over time, as the behavior of the MIRI imager at these wavelengths is better characterized.

### 2.2 Deprojection

In Supplementary Figure 10, the flux contour profiles of the disks at  $15.5$  and  $25.5\ \mu\text{m}$  are compared, chosen at logarithmic levels. We forego the contour analysis of the  $23.0\ \mu\text{m}$  data, as it is clipped both at the outer and inner regions and it is characteristically the same as the  $25.5\ \mu\text{m}$  data where they overlap. Keplerian orbits were fitted to these contours via Markov chain Monte Carlo (MCMC) fitting methods, using emcee, allowing for joint Bayesian errors to be estimated. The orbital parameters were determined using 6000 test chains with 10000 steps, allowing for a burn-in limit of 200 steps. Additionally, we determined the orientation of the system by fitting 51 points chosen by eye at the inner edge of the KBA ring with the same orbit fitting method as for the contours. This was necessary, as the contour levels track locations of equal illumination, which do not necessarily correspond to orbital paths due to the higher eccentricity and inclination of the KBA ring. The system orientation determined using the outer ring inner gap is similar to that calculated based on ALMA data ([MacGregor et al, 2017](#)), although with an inclination higher by  $\sim 2^\circ$ . We summarize the inner gap and contour fits in Supplementary Table 3.

The fitting reveals an inner disk mostly aligned with the outer KBA ring; however, there is a gradual misalignment between the disk components, with the inner disk offset by  $\sim 6.7^\circ$  in position angle relative

Flux contour lines at  $15.5 \mu\text{m}$  (blue) and  $25.5 \mu\text{m}$  (red).



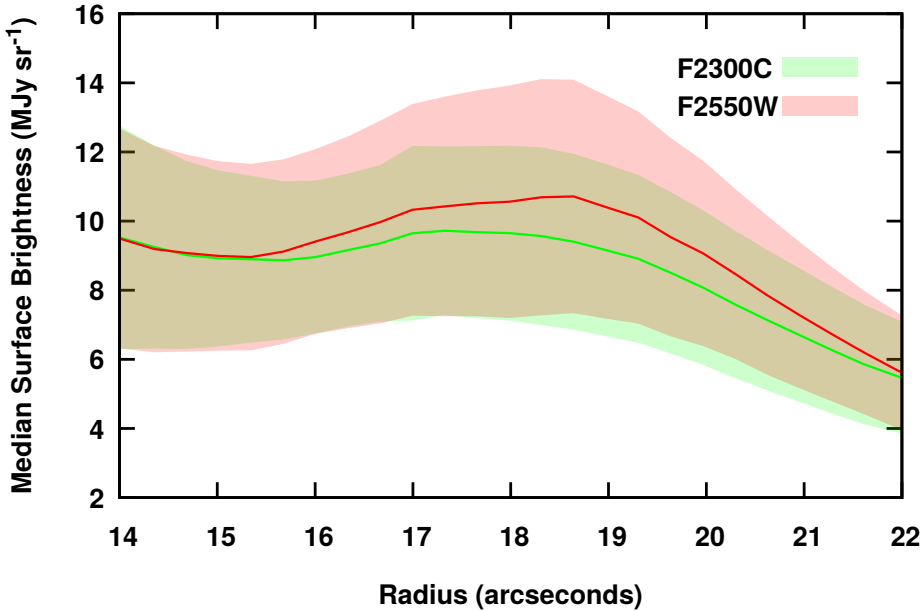
**Supplementary Figure 10** The F1550C lines are drawn at  $3.16, 10, 31.6, 100$ , and  $316 \text{ MJy sr}^{-1}$ , while the F2550W lines are drawn at  $10, 31.6, 100$ , and  $316 \text{ MJy sr}^{-1}$ . Vector lines are drawn following along the position angle of the disks ( $336.04^\circ$  and  $329.59^\circ$ ), to highlight the offsets between the inner and outer regions. Note that the F1550C and the F2550W contours align well within the ABA region.

**Supplementary Table 3** The fitted orbital parameters of the KBA inner gap and that of the contour levels shown in Supplementary Figure 10.

Flux ( $\text{MJy sr}^{-1}$ )	a (au)	e	PA (deg)	$\iota$ (deg)	$\omega$ (deg)
KBA inner gap - used for de-projection					
KBA gap	$133.79 \pm 0.26$	$0.132 \pm 0.002$	$336.28 \pm 0.09$	$67.52 \pm 0.09$	$38.04 \pm 0.8$
F1550C					
3.16	$66.38 \pm 0.08$	$0.037 \pm 0.001$	$326.22 \pm 0.09$	$56.94 \pm 0.08$	$170.72 \pm 1.75$
10.0	$44.63 \pm 0.09$	$0.028 \pm 0.002$	$326.50 \pm 0.17$	$56.19 \pm 0.15$	$161.42 \pm 4.10$
31.6	$25.86 \pm 0.11$	$0.022 \pm 0.004$	$327.79 \pm 0.62$	$44.17 \pm 0.43$	$142.56 \pm 9.80$
100.0	$14.63 \pm 0.14$	$0.020 \pm 0.008$	$328.72 \pm 2.01$	$36.23 \pm 1.23$	$161.51 \pm 24.03$
F2550W					
10.0	$172.48 \pm 0.05$	$0.020 \pm 0.001$	$336.04 \pm 0.02$	$64.42 \pm 0.02$	$5.42 \pm 0.85$
31.6	$74.35 \pm 0.07$	$0.131 \pm 0.001$	$326.71 \pm 0.09$	$52.07 \pm 0.08$	$176.37 \pm 0.43$
100	$40.23 \pm 0.09$	$0.045 \pm 0.002$	$329.59 \pm 0.28$	$47.80 \pm 0.21$	$149.65 \pm 2.61$
316	$23.36 \pm 0.12$	$0.045 \pm 0.004$	$332.01 \pm 0.77$	$43.09 \pm 0.51$	$129.52 \pm 5.50$

Semi-major axis lengths were calculated using a pixel scale of  $0.11''/\text{px}$  and a distance of  $7.7 \text{ pc}$ . The fits and joint errors were determined with emcee using the Markov chain Monte Carlo fitting algorithm assuming Keplerian orbits. The KBA gap fit results were used to de-project the images.

## The median surface brightness of the KBA ring



**Supplementary Figure 11** The median surface brightness is measured on the deprojected images, centered on coordinates  $22^{\text{h}}57^{\text{m}}39\overset{\text{s}}{.}62$ ,  $-29^{\circ}37'22\overset{\text{s}}{.}06$  (not on Fomalhaut) at the time of the observations. Statistical errors were negligible. The dominant systematic errors are based on PSF subtraction scalings with a conservative 5% and 10% additional error added in quadrature at  $25.5$  and  $23.0$   $\mu\text{m}$ , respectively.

to the KBA ring. The outer ring has a position angle of  $\sim 336^\circ$  and inclination of  $64.4^\circ$  (determined at the  $10.0$   $\text{MJy sr}^{-1}$  contour), while the inner disk is oriented at  $\sim 329.6^\circ$  with a much smaller inclination angle of  $47.8^\circ$ . In general, the position angles of the inner components are smaller than for the outer with the inclination angles also decreasing inwards. The inner disk alignment agrees at  $15.5$  and  $25.5$   $\mu\text{m}$ , demonstrating that the misalignment is not due to the PSF residuals of the 4QPM. The outermost  $15.5$   $\mu\text{m}$  contour profile is affected by the 4QPM PSF residuals, therefore any further misalignment it presents was ignored. Gravitational perturbations by a massive planet within the disk system could have plausibly carved the secondary disk gap in the system and forced this misalignment.

### 2.3 The Kuiper-belt analog

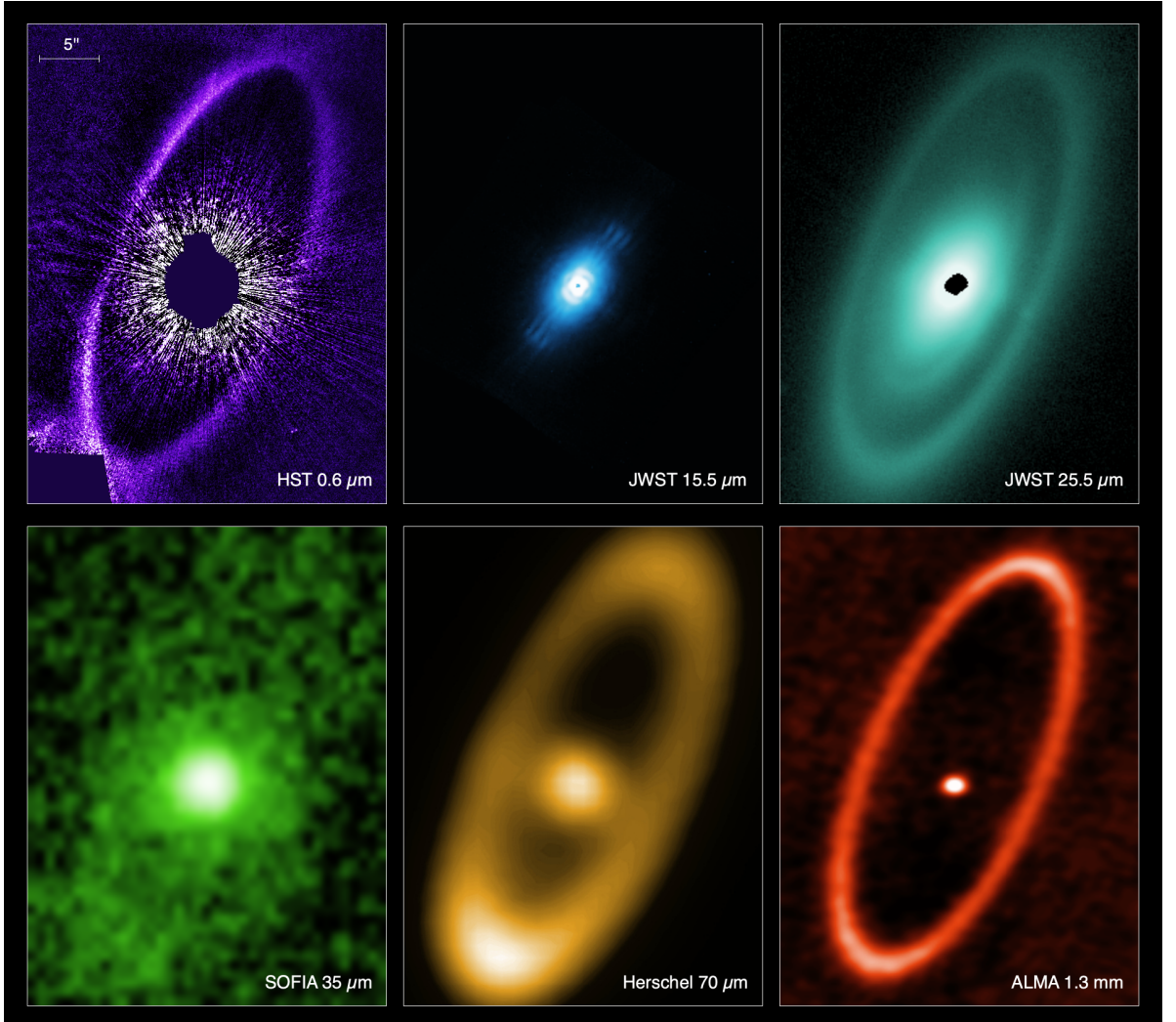
The most extended component of the Fomalhaut debris disk system is its large and narrow KBA ring. First resolved in scattered light with HST/ACS (Kalas et al, 2005), the outer ring has since been imaged at many wavelengths. Here, we report only on the observations of this component with JWST/MIRI at  $23$  and  $25.5$   $\mu\text{m}$  as it was not detected in the observations at  $15.5$   $\mu\text{m}$ . As measured on the deprojected F2550W image, the KBA ring has a sharp inner edge with a semi-major axis of  $133.8$  au and a width of approximately  $20$ - $25$  au. We measure an eccentricity of  $e = 0.132 \pm 0.002$  for the inner edge, in agreement with previous estimates (e.g.  $e = 0.12 \pm 0.01$ ; MacGregor et al, 2017). Given Fomalhaut's  $16.63$   $L_\odot$  luminosity, the thermal location of the KBA ring corresponds to an equivalent of  $30$  -  $40$  au around the Sun, establishing this ring as a true analog of the Kuiper belt.

We show the median radial profile of the ring in Supplementary Figure 11 at  $23.0$  and  $25.5$   $\mu\text{m}$ , using the de-projected image shown in main text Figure 2. We determine the radial profile centered on coordinates  $22^{\text{h}}57^{\text{m}}39\overset{\text{s}}{.}62$ ,  $-29^{\circ}37'22\overset{\text{s}}{.}06$ , which is the center of the KBA ring in the deprojected image at the observation epoch (not the location of Fomalhaut). The median peak surface brightness of the ring is  $9.7 \pm 2.4$   $\text{MJy sr}^{-1}$  at  $23.0$  and  $10.7 \pm 3.4$   $\text{MJy sr}^{-1}$  at  $25.5$   $\mu\text{m}$ . The complete disk was not imaged in the

Lyot coronagraphic subarray, but we can extrapolate an estimated total disk brightness of  $114 \pm 12$  mJy at  $23.0 \mu\text{m}$  and measured a value of  $126 \pm 9$  mJy at  $25.5 \mu\text{m}$  between  $15''.25$  (117 au) and  $20''.1$  (155 au) from this central location in the deprojected image. These flux values provide the specific total flux from the disk component itself to allow for detailed modeling. An extended blow-out halo is quite apparent in both the HST scattered light and  $25.5 \mu\text{m}$  thermal images at the two apices. In the halo, outside of  $20''.1$ , we measure a total brightness of  $126 \pm 13$  mJy at  $25.5 \mu\text{m}$ , which is just as much as within the KBA ring itself. The majority of this halo flux originates from the regions near the KBA ring.

## 2.4 The panchromatic imaging gallery of the Fomalhaut debris disk system

The panchromatic gallery of Fomalhaut observations



**Supplementary Figure 12** The images are from the following studies: HST/STIS - (Kalas et al, 2013; Gáspár and Rieke, 2020), JWST/MIRI - this work, SOFIA/FORECAST - (Adams et al, 2018), Herschel/PACS - (Acke et al, 2012), ALMA - (MacGregor et al, 2017). The gallery shows how different wavelengths highlight different regions within the disk and how JWST is uniquely able to resolve structures within the inner regions. Images are displayed at their proper orientations, with N to the top and E to the left.

The latest JWST observations of the Fomalhaut system complete the panchromatic spatially resolved imaging of the system. We would be remiss if we didn't use this opportunity to present the reader with said gallery, allowing a detailed view of dust scattered light and thermal emission from optical, through mid-IR to radio wavelengths. In Supplementary Figure 12 we present the images from HST/STIS (Kalas et al, 2013; Gáspár and Rieke, 2020, this work), MIRI (this work), SOFIA/FORECAST (Adams et al, 2018), Herschel PACS (Acke et al, 2012), and ALMA (MacGregor et al, 2017). We note that these are not the only images of the system (e.g. there are also HST/ACS images as well as Spitzer/MIPS images; Kalas et al, 2005; Stapelfeldt et al, 2004), but are the deepest, highest spatial resolution, and most complete observations at the given wavelengths. These images highlight the unique diagnostic capability of each instrument/observatory and the unparalleled opportunity we have with JWST to study such systems at mid-IR wavelengths at high spatial resolution.

## 2.5 Re-calibration of the IRS spectrum of the inner debris system

The IRS spectrum of the debris system in Su et al (2013) shows  $\sim 320$  mJy of emission at  $15\ \mu\text{m}$  from the inner debris system, whereas the coronagraphic results at  $15.5\ \mu\text{m}$  reveal “only”  $78 \pm 35$  mJy. As shown in main text Figure 5, when the spectrum is averaged over the filter bandpass, there is a very significant discrepancy.

To explore this offset, we have re-evaluated the spectrum. To do so, we use photometry of the inner system. Three of the measurements we use were obtained with beams of diameter  $6 - 10''$  van der Blieck et al (1996); Ishihara et al (2010); Su et al (2016); Adams et al (2018), i.e., all refer to the inner system. A fourth measurement utilized the synthetic photometry on the Spitzer IRS low-resolution spectrum from PID 1074 (reduction from the NASA/IPAC Infrared Science Archive, IRSA) to generate a value at  $22\ \mu\text{m}$ , again with a beam of  $\sim 8.5''$ . A summary of the results is plotted in main text Figure 5.

We now describe how the values were obtained. Measurements at 2 to  $8\ \mu\text{m}$  are reported by Su et al (2013). They conclude that there is no evidence for an excess between 2 and  $8\ \mu\text{m}$ , other than the hot excess of  $0.88 \pm 0.12\%$  at  $2\ \mu\text{m}$  detected interferometrically (Absil et al, 2009). Photometry in the  $10\ \mu\text{m}$  atmospheric window was obtained by van der Blieck et al (1996). We focus on the intermediate width ( $\Delta\lambda/\lambda \sim 0.1$ ) bands at 8.361, 9.787, and  $12.819\ \mu\text{m}$ ; although measurements in the full N-band are also reported, various types of systematic errors should be lower in the narrower bands, particularly given the peculiar transmission profile of the N-band filter used. Measurements in the intermediate bands were obtained on six nights, and the averages have indicated errors  $\leq 1\%$ . The magnitudes quoted for these measurements are based on solar colors, calculated from the solar spectrum in Labs and Neckel (1970). These colors are rather far from current understanding, so we computed colors across the three intermediate bands using the spectra of Sirius and the Sun in Rieke et al (2023a). Correcting to these colors and adopting the given magnitude at the shortest band, the magnitudes are: 0.916 ( $8.361\ \mu\text{m}$ ), 0.890 ( $9.787\ \mu\text{m}$ ), and 0.903 ( $12.819\ \mu\text{m}$ ). We average the first two to get 0.901 and assume, based on the IRAC measurements, that there is no excess in those bands. The value in the third band then shows no excess there either. Given the nominal error of 3% but the relatively large number of measurements in the intermediate bands and their resistance to systematic errors, we assign an error of 2%.

Our measurement of the Fomalhaut debris disk contribution at  $18\ \mu\text{m}$  is based on a self-calibrating use of the  $9$  and  $18\ \mu\text{m}$  photometry from Akari. We first used Su et al (2006) to identify A-stars with no evidence for excess emission at  $24\ \mu\text{m}$  and that are bright enough to be measured at high signal-to-noise in the two Akari bands. The stars passing these two tests are HD 11636, 76644, 80007, 87901, 103287, 108767, 112185, 130841, 135742, 209952, and 216627. We assumed all of these stars had the identical ratio of  $9$  to  $18\ \mu\text{m}$  flux densities. In addition to the tabulated statistical errors, we assigned an error parameter for additional errors in the photometry. We found that, if this additional error was set to 2.5%, that  $\chi^2$  for the average was 1. We took the weighted average of the determinations with this additional error. When compared with the average of the fluxes in the two bands for Fomalhaut, this implies an excess for it at  $18\ \mu\text{m}$  of  $280 \pm 95$  mJy.

We used a technique similar to that for the Akari data to derive the 22  $\mu\text{m}$  result. The extraction aperture for the IRS spectrum (from PID 1074, IRS) and hence the synthetic photometry based on it is  $\sim 8.5''$ , closely comparable to that for the measurements at 12.8 and 24  $\mu\text{m}$ . We determined the average ratio of the 22  $\mu\text{m}$  to 16  $\mu\text{m}$  photometry for A-stars without excess (Sloan et al, 2015), namely HR 1251, 3799, 4138, 4801, 6789, and 7950. Making a small correction for excess in the 16  $\mu\text{m}$  band, the excess above the stellar photospheric output at 22  $\mu\text{m}$  compared with these non-excess stars is indicated to be  $13.8 \pm 2.8\%$ , or a flux of  $540 \pm 110$  mJy.

Measurements at 24 and 37  $\mu\text{m}$  were taken from Su et al (2016) and Adams et al (2018). Except for the last case, all were adjusted to the calibration of Rieke et al (2023a). We then used these four measurements to renormalize the spectrum. In addition to the statistical errors for the spectral points, we assumed an error of 0.5% of the stellar photosphere at 10  $\mu\text{m}$ , increasing linearly with wavelength (as  $\lambda/10 \mu\text{m}$ ) toward longer wavelengths, to allow for uncertainties in the stellar SED (e.g., due to the hot dust emission, Absil et al, 2009; Mennesson et al, 2013). The normalization is achieved by adjusting the calibration of the spectrum before subtracting the stellar continuum. Because one is subtracting a large number (the spectrum of star plus excess) from another large one (the photospheric emission) to get a smaller one (the spectrum of the excess), the normalization is very sensitive to the overall calibration of the spectrum. The result needs to be consistent with the four shorter-wavelength photometric points and to not go too far negative at the shortest wavelengths near 10  $\mu\text{m}$ .

Nonetheless, the derived excess spectrum does go somewhat negative short of 13  $\mu\text{m}$ . As an independent test, we have used the IRS spectrum from PID 1074; although it is saturated at wavelengths less than 10  $\mu\text{m}$ , it is valid at the longer wavelengths. We normalized this spectrum so that, after subtracting the photospheric continuum, the average excess indicated between 10 and 14  $\mu\text{m}$  is equal to zero. As shown in main text Figure 5, the derived excess spectrum shows no gradient over this wavelength range, supporting the assignment of no excess (since any plausible excess would have a redder spectrum than the stellar photospheric one). Furthermore, the spectrum of the excess agrees closely with that from the renormalized one from Su et al (2013). (Beyond 30  $\mu\text{m}$ , the PID 1074 spectrum becomes more noisy and as indicated in the figure departs systematically from the spectrum from Su et al (2013), which overall should be the more reliable of the two.)

## References

- Absil O, Mennesson B, Le Bouquin JB, et al (2009) An Interferometric Study of the Fomalhaut Inner Debris Disk. I. Near-Infrared Detection of Hot Dust with VLTI/VINCI. *Astrophys. J.* 704(1):150–160. <https://doi.org/10.1088/0004-637X/704/1/150>, <https://arxiv.org/abs/arXiv:0908.3133> [astro-ph.SR]
- Acke B, Min M, Dominik C, et al (2012) Herschel images of Fomalhaut. An extrasolar Kuiper belt at the height of its dynamical activity. *Astron. Astrophys.* 540:A125. <https://doi.org/10.1051/0004-6361/201118581>, <https://arxiv.org/abs/arXiv:1204.5037> [astro-ph.SR]
- Adams JD, Herter TL, Lau RM, et al (2018) Dust Production Rates in the Fomalhaut Debris Disk from SOFIA/FORCAST Mid-infrared Imaging. *Astrophys. J.* 862(2):161. <https://doi.org/10.3847/1538-4357/aacf96>, <https://arxiv.org/abs/arXiv:1806.09746> [astro-ph.EP]
- Apai D, Schneider G, Grady CA, et al (2015) The Inner Disk Structure, Disk-Planet Interactions, and Temporal Evolution in the  $\beta$  Pictoris System: A Two-epoch HST/STIS Coronagraphic Study. *Astrophys. J.* 800(2):136. <https://doi.org/10.1088/0004-637X/800/2/136>, <https://arxiv.org/abs/arXiv:1501.03181> [astro-ph.EP]
- Aumann HH, Beichman CA, Gillett FC, et al (1984) Discovery of a shell around Alpha Lyrae. *Astrophys. J. Lett.* 278:L23–L27. <https://doi.org/10.1086/184214>
- Ballering NP, Rieke GH, Gáspár A (2014) Probing the Terrestrial Regions of Planetary Systems: Warm Debris Disks with Emission Features. *Astrophys. J.* 793:57. <https://doi.org/10.1088/0004-637X/793/1/57>, <https://arxiv.org/abs/arXiv:1407.7547> [astro-ph.EP]
- Ballering NP, Rieke GH, Su KYL, et al (2017) What Sets the Radial Locations of Warm Debris Disks? *Astrophys. J.* 845(2):120. <https://doi.org/10.3847/1538-4357/aa8037>, <https://arxiv.org/abs/arXiv:1708.07151> [astro-ph.EP]
- Boccaletti A, Riaud P, Baudoz P, et al (2004) The Four-Quadrant Phase Mask Coronagraph. IV. First Light at the Very Large Telescope. *Publ. Astron. Soc. Pac.* 116(825):1061–1071. <https://doi.org/10.1086/425735>
- Boccaletti A, Lagage PO, Baudoz P, et al (2015) The Mid-Infrared Instrument for the James Webb Space Telescope, V: Predicted Performance of the MIRI Coronagraphs. *Publ. Astron. Soc. Pac.* 127(953):633. <https://doi.org/10.1086/682256>, <https://arxiv.org/abs/arXiv:1508.02352> [astro-ph.IM]
- Boccaletti A, Cossou C, Baudoz P, et al (2022) JWST/MIRI coronagraphic performances as measured on-sky. *Astron. Astrophys.* 667:A165. <https://doi.org/10.1051/0004-6361/202244578>, <https://arxiv.org/abs/arXiv:2207.11080> [astro-ph.IM]
- Boley AC, Payne MJ, Corder S, et al (2012) Constraining the Planetary System of Fomalhaut Using High-resolution ALMA Observations. *Astrophys. J. Lett.* 750:L21. <https://doi.org/10.1088/2041-8205/750/1/L21>, <https://arxiv.org/abs/arXiv:1204.0007> [astro-ph.EP]
- Bouchet P, García-Marín M, Lagage PO, et al (2015) The Mid-Infrared Instrument for the James Webb Space Telescope, III: MIRIM, The MIRI Imager. *Publ. Astron. Soc. Pac.* 127(953):612. <https://doi.org/10.1086/682254>, <https://arxiv.org/abs/arXiv:1508.02488> [astro-ph.IM]
- Carter AL, Hinkley S, Kammerer J, et al (2022) The JWST Early Release Science Program for Direct Observations of Exoplanetary Systems I: High Contrast Imaging of the Exoplanet HIP 65426 b from 2–16  $\mu$ m. *arXiv e-prints arXiv:2208.14990*. <https://arxiv.org/abs/arXiv:2208.14990> [astro-ph.EP]

- Chiang E, Kite E, Kalas P, et al (2009) Fomalhaut's Debris Disk and Planet: Constraining the Mass of Fomalhaut b from disk Morphology. *Astrophys. J.*693:734–749. <https://doi.org/10.1088/0004-637X/693/1/734>, <https://arxiv.org/abs/arXiv:0811.1985>
- Draine BT, Lee HM (1984) Optical properties of interstellar graphite and silicate grains. *Astrophys. J.*285:89–108. <https://doi.org/10.1086/162480>
- Espinoza P, Su K, Rieke G, et al (2011) Discovery of an Extended Halo in the Fomalhaut Debris System. In: American Astronomical Society Meeting Abstracts #217, p 339.01
- Esposito TM, Kalas P, Fitzgerald MP, et al (2020) Debris Disk Results from the Gemini Planet Imager Exoplanet Survey's Polarimetric Imaging Campaign. *Astron. J.*160(1):24. <https://doi.org/10.3847/1538-3881/ab9199>, <https://arxiv.org/abs/arXiv:2004.13722> [astro-ph.EP]
- Faramaz V, Marino S, Booth M, et al (2021) A Detailed Characterization of HR 8799's Debris Disk with ALMA in Band 7. *Astron. J.* 161(6):271. <https://doi.org/10.3847/1538-3881/abf4e0>, <https://arxiv.org/abs/arXiv:2104.02088> [astro-ph.EP]
- Galicher R, Marois C, Zuckerman B, et al (2013) Fomalhaut b: Independent Analysis of the Hubble Space Telescope Public Archive Data. *Astrophys. J.*769(1):42. <https://doi.org/10.1088/0004-637X/769/1/42>, <https://arxiv.org/abs/arXiv:1210.6745> [astro-ph.EP]
- Gáspár A, Rieke G (2020) New HST data and modeling reveal a massive planetesimal collision around Fomalhaut. *Proc. Natl Acad. Sci. USA*117(18):9712–9722. <https://doi.org/10.1073/pnas.1912506117>, <https://arxiv.org/abs/arXiv:2004.08736> [astro-ph.EP]
- Gáspár A, Psaltis D, Özel F, et al (2012) Modeling Collisional Cascades in Debris Disks: The Numerical Method. *Astrophys. J.*749:14. <https://doi.org/10.1088/0004-637X/749/1/14>, <https://arxiv.org/abs/arXiv:1110.5929> [astro-ph.SR]
- Gauchet L, Lacour S, Lagrange AM, et al (2016) Sparse aperture masking at the VLT. II. Detection limits for the eight debris disks stars  $\beta$  Pic, AU Mic, 49 Cet,  $\eta$  Tel, Fomalhaut, g Lup, HD 181327 and HR 8799. *Astron. Astrophys.* 595:A31. <https://doi.org/10.1051/0004-6361/201526404>, <https://arxiv.org/abs/arXiv:1606.08498> [astro-ph.EP]
- Geiler F, Krivov AV (2017) Does warm debris dust stem from asteroid belts? *Mon. Not. R. Astron. Soc.*468(1):959–970. <https://doi.org/10.1093/mnras/stx462>, <https://arxiv.org/abs/arXiv:1702.05966> [astro-ph.EP]
- Gillett FC (1986) IRAS observations of cool excess around main sequence stars. In: F. P. Israel (ed) Light on Dark Matter, pp 61–69
- Holland WS, Greaves JS, Zuckerman B, et al (1998) Submillimetre images of dusty debris around nearby stars. *Nature*392:788–791. <https://doi.org/10.1038/33874>
- Holland WS, Greaves JS, Dent WRF, et al (2003) Submillimeter Observations of an Asymmetric Dust Disk around Fomalhaut. *Astrophys. J.*582:1141–1146. <https://doi.org/10.1086/344819>
- Ishihara D, Onaka T, Kataza H, et al (2010) The AKARI/IRC mid-infrared all-sky survey. *Astron. Astrophys.*514:A1. <https://doi.org/10.1051/0004-6361/200913811>, <https://arxiv.org/abs/arXiv:1003.0270> [astro-ph.IM]
- Jansen RA, Collins NR, Windhorst RA (2003) Autofilet.pro: An Improved Method for Automated

Removal of Herring-bone Pattern Noise from CCD Data. In: HST Calibration Workshop : Hubble after the Installation of the ACS and the NICMOS Cooling System, p 193

Janson M, Carson JC, Lafrenière D, et al (2012) Infrared Non-detection of Fomalhaut b: Implications for the Planet Interpretation. *Astrophys. J.* 747(2):116. <https://doi.org/10.1088/0004-637X/747/2/116>, <https://arxiv.org/abs/arXiv:1201.4388> [astro-ph.EP]

Kalas P, Graham JR, Clampin M (2005) A planetary system as the origin of structure in Fomalhaut's dust belt. *Nature* 435(7045):1067–1070. <https://doi.org/10.1038/nature03601>, <https://arxiv.org/abs/arXiv:astro-ph/0506574> [astro-ph]

Kalas P, Graham JR, Chiang E, et al (2008) Optical Images of an Exosolar Planet 25 Light-Years from Earth. *Science* 322(5906):1345. <https://doi.org/10.1126/science.1166609>, <https://arxiv.org/abs/arXiv:0811.1994> [astro-ph]

Kalas P, Graham JR, Fitzgerald MP, et al (2013) STIS Coronagraphic Imaging of Fomalhaut: Main Belt Structure and the Orbit of Fomalhaut b. *Astrophys. J.* 775(1):56. <https://doi.org/10.1088/0004-637X/775/1/56>, <https://arxiv.org/abs/arXiv:1305.2222> [astro-ph.EP]

Kammerer J, Girard J, Carter AL, et al (2022) Performance of near-infrared high-contrast imaging methods with JWST from commissioning. In: Coyle LE, Matsuura S, Perrin MD (eds) Space Telescopes and Instrumentation 2022: Optical, Infrared, and Millimeter Wave, p 121803N, <https://doi.org/10.1117/12.2628865>, [2208.00996](https://arxiv.org/abs/2208.00996)

Kennedy GM, Wyatt MC (2011) Collisional evolution of irregular satellite swarms: detectable dust around Solar system and extrasolar planets. *Mon. Not. R. Astron. Soc.* 412(4):2137–2153. <https://doi.org/10.1111/j.1365-2966.2010.18041.x>, <https://arxiv.org/abs/arXiv:1011.4858> [astro-ph.EP]

Kennedy GM, Wyatt MC (2014) Do two-temperature debris discs have multiple belts? *Mon. Not. R. Astron. Soc.* 444:3164–3182. <https://doi.org/10.1093/mnras/stu1665>, <https://arxiv.org/abs/arXiv:1408.4116> [astro-ph.EP]

Kenworthy MA, Meshkat T, Quanz SP, et al (2013) Coronagraphic Observations of Fomalhaut at Solar System Scales. *Astrophys. J.* 764(1):7. <https://doi.org/10.1088/0004-637X/764/1/7>, <https://arxiv.org/abs/arXiv:1212.1459> [astro-ph.SR]

Kenyon SJ, Bromley BC (2015) Collisional Cascade Calculations for Irregular Satellite Swarms in Fomalhaut b. *Astrophys. J.* 811(1):60. <https://doi.org/10.1088/0004-637X/811/1/60>, <https://arxiv.org/abs/arXiv:1508.03350> [astro-ph.EP]

Kenyon SJ, Currie T, Bromley BC (2014) Fomalhaut b as A Cloud of Dust: Testing Aspects of Planet Formation Theory. *Astrophys. J.* 786(1):70. <https://doi.org/10.1088/0004-637X/786/1/70>, <https://arxiv.org/abs/arXiv:1403.5268> [astro-ph.SR]

Labs D, Neckel H (1970) Transformation of the absolute solar radiation data into the ‘International Practical Temperature Scale of 1968’. *Sol. Phys.* 15(1):79–87. <https://doi.org/10.1007/BF00149474>

Lawler SM, Greenstreet S, Gladman B (2015) Fomalhaut b as a Dust Cloud: Frequent Collisions within the Fomalhaut Disk. *Astrophys. J. Lett.* 802(2):L20. <https://doi.org/10.1088/2041-8205/802/2/L20>, <https://arxiv.org/abs/arXiv:1412.1129> [astro-ph.EP]

Lebreton J, van Lieshout R, Augereau JC, et al (2013) An interferometric study of the Fomalhaut inner debris disk. III. Detailed models of the exozodiacal disk and its origin. *Astron. Astrophys.* 555:A146.

- <https://doi.org/10.1051/0004-6361/201321415>, <https://arxiv.org/abs/arXiv:1306.0956> [astro-ph.EP]
- MacGregor MA, Wilner DJ, Rosenfeld KA, et al (2013) Millimeter Emission Structure in the First ALMA Image of the AU Mic Debris Disk. *Astrophys. J. Lett.* 762(2):L21. <https://doi.org/10.1088/2041-8205/762/2/L21>, <https://arxiv.org/abs/arXiv:1211.5148> [astro-ph.EP]
- MacGregor MA, Matrà L, Kalas P, et al (2017) A Complete ALMA Map of the Fomalhaut Debris Disk. *Astrophys. J.* 842(1):8. <https://doi.org/10.3847/1538-4357/aa71ae>, <https://arxiv.org/abs/arXiv:1705.05867> [astro-ph.EP]
- Maire AL, Boccaletti A, Rameau J, et al (2014) Search for cool giant exoplanets around young and nearby stars. VLT/NaCo near-infrared phase-coronagraphic and differential imaging. *Astron. Astrophys.* 566:A126. <https://doi.org/10.1051/0004-6361/201323084>, <https://arxiv.org/abs/arXiv:1404.3502> [astro-ph.EP]
- Marois C, Macintosh B, Barman T, et al (2008) Direct Imaging of Multiple Planets Orbiting the Star HR 8799. *Science* 322:1348–. <https://doi.org/10.1126/science.1166585>, <https://arxiv.org/abs/arXiv:0811.2606>
- Mennesson B, Absil O, Lebreton J, et al (2013) An Interferometric Study of the Fomalhaut Inner Debris Disk. II. Keck Nuller Mid-infrared Observations. *Astrophys. J.* 763(2):119. <https://doi.org/10.1088/0004-637X/763/2/119>, <https://arxiv.org/abs/arXiv:1211.7143> [astro-ph.SR]
- Morales FY, Rieke GH, Werner MW, et al (2011) Common Warm Dust Temperatures Around Main-sequence Stars. *Astrophys. J. Lett.* 730:L29. <https://doi.org/10.1088/2041-8205/730/2/L29>
- Perrin MD, Sivaramakrishnan A, Lajoie CP, et al (2014) Updated point spread function simulations for JWST with WebbPSF. In: Oschmann JJacobus M., Clampin M, Fazio GG, et al (eds) Space Telescopes and Instrumentation 2014: Optical, Infrared, and Millimeter Wave, p 91433X, <https://doi.org/10.1117/12.2056689>
- Quillen AC (2006) Predictions for a planet just inside Fomalhaut's eccentric ring. *Mon. Not. R. Astron. Soc.* 372(1):L14–L18. <https://doi.org/10.1111/j.1745-3933.2006.00216.x>, <https://arxiv.org/abs/arXiv:astro-ph/0605372> [astro-ph]
- Ren B, Wang JJ, Pueyo L (2019) centerRadon: Center determination code in stellar images. *Astrophysics Source Code Library*, record ascl:1906.021, [1906.021](https://ascl.net/1906.021)
- Ressler ME, Cho H, Lee RAM, et al (2008) Performance of the JWST/MIRI Si:As detectors. In: Dorn DA, Holland AD (eds) High Energy, Optical, and Infrared Detectors for Astronomy III, p 70210O, <https://doi.org/10.1117/12.789606>
- Rhee JH, Song I, Zuckerman B, et al (2007) Characterization of Dusty Debris Disks: The IRAS and Hipparcos Catalogs. *Astrophys. J.* 660(2):1556–1571. <https://doi.org/10.1086/509912>, <https://arxiv.org/abs/arXiv:astro-ph/0609555> [astro-ph]
- Ricci L, Carpenter JM, Fu B, et al (2015) ALMA Observations of the Debris Disk around the Young Solar Analog HD 107146. *Astrophys. J. Lett.* 798(2):L24. <https://doi.org/10.1088/0004-637X/798/2/L24>, <https://arxiv.org/abs/arXiv:1410.8265> [astro-ph.EP]
- Rieke GH, Engelke C, Su K, et al (2023a) Absolute Calibration. III. Improved Absolute Calibration for the Visible through the Mid-infrared. *Astron. J.* 165(3):99. <https://doi.org/10.3847/1538-3881/ac9f1b>

- Rieke MJ, Kelly DM, Misselt K, et al (2023b) Performance of NIRCam on JWST in Flight. *Publ. Astron. Soc. Pac.*135(1044):028001. <https://doi.org/10.1088/1538-3873/acac53>
- Rigby J, Perrin M, McElwain M, et al (2022) The Science Performance of JWST as Characterized in Commissioning. arXiv e-prints arXiv:2207.05632. <https://arxiv.org/abs/arXiv:2207.05632> [astro-ph.IM]
- Roman NG (1959) Planets of other suns. *Astron. J.*64:344–345. <https://doi.org/10.1086/108038>
- Rouan D, Riaud P, Boccaletti A, et al (2000) The Four-Quadrant Phase-Mask Coronagraph. I. Principle. *Publ. Astron. Soc. Pac.*112(777):1479–1486. <https://doi.org/10.1086/317707>
- Sloan GC, Herter TL, Charmandaris V, et al (2015) Spectral Calibration in the Mid-Infrared: Challenges and Solutions. *Astron. J.*149(1):11. <https://doi.org/10.1088/0004-6256/149/1/11>, <https://arxiv.org/abs/arXiv:1408.5922> [astro-ph.SR]
- Soummer R, Pueyo L, Larkin J (2012) Detection and Characterization of Exoplanets and Disks Using Projections on Karhunen-Loève Eigenimages. *Astrophys. J. Lett.*755(2):L28. <https://doi.org/10.1088/2041-8205/755/2/L28>, <https://arxiv.org/abs/arXiv:1207.4197> [astro-ph.IM]
- Stapelfeldt KR, Holmes EK, Chen C, et al (2004) First Look at the Fomalhaut Debris Disk with the Spitzer Space Telescope. *Astrophys. J. Suppl. Ser.*154:458–462. <https://doi.org/10.1086/423135>
- Su KYL, Rieke GH (2014) Signposts of Multiple Planets in Debris Disks. In: Booth M, Matthews BC, Graham JR (eds) Exploring the Formation and Evolution of Planetary Systems, pp 318–321, <https://doi.org/10.1017/S1743921313008764>, 1307.1735
- Su KYL, Rieke GH, Stansberry JA, et al (2006) Debris Disk Evolution around A Stars. *Astrophys. J.*653:675–689. <https://doi.org/10.1086/508649>, <https://arxiv.org/abs/arXiv:astro-ph/0608563>
- Su KYL, Rieke GH, Malhotra R, et al (2013) Asteroid Belts in Debris Disk Twins: Vega and Fomalhaut. *Astrophys. J.*763:118. <https://doi.org/10.1088/0004-637X/763/2/118>, <https://arxiv.org/abs/arXiv:1301.1331> [astro-ph.EP]
- Su KYL, Rieke GH, Defrére D, et al (2016) The Inner Debris Structure in the Fomalhaut Planetary System. *Astrophys. J.*818(1):45. <https://doi.org/10.3847/0004-637X/818/1/45>, <https://arxiv.org/abs/arXiv:1512.03535> [astro-ph.EP]
- van der Blieck NS, Manfroid J, Bouchet P (1996) Infrared aperture photometry at ESO (1983-1994) and its future use. *Astron. Astrophys. Suppl.*119:547–557
- van Leeuwen F (2007) Validation of the new Hipparcos reduction. *Astron. Astrophys.*474(2):653–664. <https://doi.org/10.1051/0004-6361:20078357>, <https://arxiv.org/abs/arXiv:0708.1752> [astro-ph]
- White SM, Iwai K, Phillips NM, et al (2017) Observing the Sun with the Atacama Large Millimeter-/submillimeter Array (ALMA): Fast-Scan Single-Dish Mapping. *Sol. Phys.*292(7):88. <https://doi.org/10.1007/s11207-017-1123-2>, <https://arxiv.org/abs/arXiv:1705.04766> [astro-ph.SR]
- Wolff SG, Gáspár A, H. Rieke G, et al (2023) Hiding Dust around  $\epsilon$  Eridani. *Astron. J.*165(3):115. <https://doi.org/10.3847/1538-3881/acac83>, <https://arxiv.org/abs/arXiv:2302.10085> [astro-ph.EP]